Additive Manufacturing 54 (2022) 102736

Contents lists available at ScienceDirect

Additive Manufacturing

journal homepage: www.elsevier.com/locate/addma

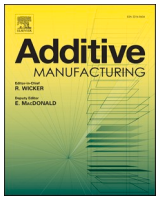

Research Paper

Detection, classification and prediction of internal defects from surface morphology data of metal parts fabricated by powder bed fusion type additive manufacturing using an electron beam

Yunwei Gui [a], Kenta Aoyagi [b,*], Huakang Bian [b], Akihiko Chiba [b]

[a] Department of Materials Processing, Graduate School of Engineering, Tohoku University, 6-6-11 Aoba, Aramaki, Aoba-ku, Sendai 980-8579, Japan
[b] Institute for Materials Research, Tohoku University, 2-1-1 Katahira, Aoba-ku, Sendai 980-8577, Japan

ARTICLE INFO

Keywords:
Additive manufacturing
Powder bed fusion
Surface morphology
Internal defects
Machine learning

ABSTRACT

In powder bed fusion type additive manufacturing using an electron beam (PBF-EB), various process parameters have a significant influence on the performance of manufactured parts. To expand the use of PBF-EB technology in the material industry, one of the problems is the generation of internal defects (pores, unmelted powder, among others) during the process. In this study, we determined a quantitative criterion (Sdr $<$ 0.015 for an even surface; Sa $\geq$ 80 μm for an uneven surface; Sdr $\geq$ 0.015 and Sa $<$ 80 μm for a porous surface) for classifying surface quality based on surface flatness, and we revealed that different surface qualities (even, uneven, and porous) include different types of internal defects. The parts with even surfaces are free of internal defects and have the highest density(7.7962 g/cm^3). Parts with uneven surfaces have a large number of spherical pores owing to their excessive energy input, while parts with porous surfaces have a considerable number of irregularly shaped defects and unmelted powders owing to their insufficient energy input. When the energy input is excessively high, the combination of the Marangoni effect, vapor recoil pressure, and electron beam agitation leads to a high velocity flow of liquid, which tends to form bumps, resulting in an uneven surface. Conversely, if the energy input is too low, the depth of the melt pool is too small to penetrate the thickness of the powder layers, resulting in incomplete melting of the powder at the bottom of the layers and the formation of defects due to lack of fusion between the layers. In addition, five types of machine learning technologies (logistic regression, support vector machine, decision tree, XGBoost, and naive Bayes) were applied to the PBF-EB process parameters optimization of the S30C alloy. A support vector machine has the highest model performance, and we use it to construct a processing map corresponding to the internal defects and determine the PBF-EB process window for the S30C alloy. The optimal PBF-EB process parameter ranges for S30C alloy were predicted as follows: current = 2.5–10 mA, scan speed = 200–1000 mm/s, line offset = 0.11–0.25 mm, or current = 2.5–10 mA, scan speed = 200–750 mm/s, line offset = 0.27–0.33 mm. Moreover, a new framework for constructing a process map of PBF-EB fabricated parts was proposed, which is an effective method to accelerate PBF-EB for manufacturing parts without internal defects.

1. Introduction

Additive manufacturing (AM) technology is a process to manufacture parts in an additive manner, not a subtractive manner, and it is achieved through the gradual accumulation of materials [1–3]. This manufacturing technology enables the manufacture of complex structures that are difficult to manufacture with conventional technology; thus, it effectively simplifies the production process and shortens the manufacturing cycle time. In recent years, in the field of AM, many types of materials have been used, forming structures have become more complex, and the forming accuracy of parts has been improved [2–5]. Among AM technologies, powder bed fusion-type AM using an electron beam (PBF-EB) is a rapidly developing AM technology. In PBF-EB technology, metal powder is melted using an electron beam, and metal parts with complex shapes are manufactured in a layer-by-layer manner [6–8]. The PBF-EB technology has the following advantages: (i) complex geometries can be directly processed; (ii) the parts can be manufactured in a near-net shape, thereby reducing subsequent

* Corresponding author.
E-mail address: kenta.aoyagi.e7@tohoku.ac.jp (K. Aoyagi).

https://doi.org/10.1016/j.addma.2022.102736
Received 4 November 2021; Received in revised form 26 January 2022; Accepted 3 March 2022
Available online 7 March 2022

processing; (iii) the process is conducted under a vacuum environment, which can avoid degradation such as oxidation and nitridation caused by melting in air; and (iv) the unmelted powder can be recycled after printing [8–10].

In PBF-EB, various parameters have a significant impact on the quality of the manufactured parts. Internal defects (porosity, unmelted powder, among others) are crucial factors that degrade the mechanical properties of PBF-EB parts [7,11,12]. It is essential for PBF technology to produce defect-free parts in a reproducible manner, and the main factors leading to porosity and high roughness in parts printed by PBF technology are process parameters, and so on [13]. To expand the use of PBF-EB technology in the material industry, an efficient and cost-effective process optimization method for eliminating internal defects needs to be developed. With the rapid developments in artificial intelligence technology, machine learning has been applied in AM in recent years [14–19], and machine learning techniques can be utilized to output new high-performance metamaterials, optimize process parameters and topology design, defect monitoring during processing, and product quality assessment and control. The use of machine learning techniques for modeling the multidimensional parameters affecting the AM process can reduce the time and cost of elucidating AM techniques and optimizing these complex, multidisciplinary crossover projects. The literature [20] investigation reveals that machine learning techniques can be effectively applied to additive manufacturing in the areas of prediction of mechanical behavior, optimizing process parameters of 3D printing, porosity prediction and defect detection in 3D-printed parts, which not only offers significant time and economic savings, but also provides the feasibility of designing microstructures with extraordinary properties. Aoyagi et al. [21] developed a novel process optimization method using a support vector machine and successfully manufactured CoCr alloy parts without internal defects. This method can significantly shorten the research cycle and reduce the development costs.

The two main types of internal defects in PBF-EB manufactured parts are gas pores and lack of fusion. The principle causes of gas pores are: hollow powder in the raw material powder; gas adsorbed on the surface of the powder which does not escape in time to be retained in the formed part during rapid solidification; and the surface flatness of the formed part which affects the quality of the powder layer [11,12,22–25]. Lack of fusion is mainly due to improper printing parameters or the unevenness of the powder layer and other reasons resulting in some areas of the powder is not completely melted and left in the formed parts of the phenomenon of unmelted powder and narrow porosity [12]. The literature survey reveals [12] that the lack of fusion defects are mainly due to poor scanning and filling procedures and the instability of the electron beam. Internal defects such as pores and lack of fusion defects can damage the mechanical and fatigue properties of the formed part and lead to premature fracture. The main studies for controlling internal defects are online monitoring of defects, remelting and hot isostatic pressing (HIP). The literatures [26,27] report the use of infrared imaging or other imaging techniques to identify defects, but the monitoring of smaller sized defects is still not adequate. And in some cases remelting does not reduce the internal defects of the part, but instead causes coarsening of the macrostructure and volatilization of some metal elements [12]. The HIP treatment does not completely eliminate the defect, the original defect location may still act as a point of origin of the crack, and the subsequent treatment will consume more time and economic costs [12]. Therefore, optimizing suitable printing parameters to avoid internal defects in printed parts at source is of great industrial value and research significance, and is an urgent issue in PBF-EB related technology. Previous studies [21,28–30] have revealed a correlation between the surface morphology and defects. This suggests that the surface morphology of a part can be used as a criterion for evaluating internal defects in additively manufactured parts. However, the quantitative relation between surface morphology and internal defects is unclear.

Steel has many advantages such as large reserves, easy reduction, low production costs, and their microstructure and mechanical properties can be controlled by the design of alloying elements and heat treatment, so it is widely used in the transportation industry and civil engineering. Carbon steel for mechanical construction is a steel material consisting mainly of iron and carbon, with small amounts of silicon and manganese as deoxidants, and phosphorus and sulfur as impurities. Steels with a carbon content of 0.3 ± 0.03 mass % are labeled S30C. In general, S10C to S25C are less hardenable and are therefore tempered before being put into practical use. PBF-EB and other additive manufacturing methods have been increasingly used in the development of high performance materials and they are also widely used in steel materials, but mainly in alloy steels such as stainless steel and tool steels, with few examples applied to low alloy and carbon steels [31–34]. Therefore, in this study, the carbon steel S30C was chosen to provide a reference for the application of AM technology to a wider range of materials.

In this study, we used 3D non-destructive inspection techniques to determine a quantitative criterion for classifying the types of internal defects. We then investigated the formation mechanisms of the surface flatness and internal defects under different processing parameters. In addition, we compared the model performance of several machine learning techniques and constructed a processing map from the datasets classified using the determined criteria. Finally, based on these results, we propose a new framework to accelerate the development of defect-free parts for PBF-EB.

2. Materials and experimental methods

2.1. Materials

The carbon steel S30C alloy powder prepared by the gas atomization method was used as a raw material for PBF-EB. The chemical composition of the S30C alloy powder is listed in Table 1. The particle size distribution of the powder was measured using a laser particle size analyzer (LS230, Beckman Coulter, USA). The surface morphology of the S30C alloy powder was observed using a scanning electron microscope (SEM; JEOL JCM-6000). The cross-sectional microstructure of the S30C alloy powder was observed using field-emission scanning electron microscopy (FE-SEM; JEOL JSM-IT800) with an electron backscattered diffraction detector (TSL-OIM, EDAX).

2.2. Fabrication and characterization of S30C parts by using PBF-EB

In the PBF-EB technique, an electron beam is used as a heat source to selectively melt and solidify a single layer of metal powder, followed by repeated stacking of multiple layers to form the desired three-dimensional structure. A schematic diagram of the PBF-EB system is shown in the Supplementary material (Fig. S1a). In this system the S30C powder is packed in a powder hopper and under gravity the powder is fed into a start plate (SUS304 base plate) on the build platform where it is raked into an approximately 75 μm thick layer. The electron beam produced by the electron gun with an accelerating voltage of 60 kV is focused by a lens system and scanned over the powder layers by a computer-aided design system. The PBF-EB process consists of four steps: (1) raking a layer powder, (2) preheating, (3) selective melting, and (4) stage down, as shown in the Supplementary material (Fig. S1b). A PBF-EB machine developed by the Technology Research Association for Future Additive Manufacturing (TRFAM) was used to fabricate S30C cube parts with a length of 15 mm, width of 15 mm, and height of 4.5 mm. A support structure with a height of 3 mm was fabricated under the parts. For this TRFAM-developed PBF-EB machine, the process parameters that we can change are layer thickness, preheating temperature, beam current, scan speed and line offset. During our preliminary experimental optimization, it was found that a layer thickness of 75 μm was more favorable for the spreading and melting of this S30C powder, and S30C powder 'smoking' behavior can be effectively avoided when the preheating temperature is around 1131 K. Therefore, the only three

Table 1
Chemical composition of the gas-atomized powder of carbon steel S30C alloy used herein.

Element	C	Si	Mn	P	S	Ni	Cr	Fe
Composition (wt%)	0.33	0.96	0.96	0.007	0.003	0.02	0.07	Bal.

parameters we can change are beam current, scan speed and line offset. Where the beam current can be used to react to the electron beam power due to the beam power is equal to the product of the beam current and the accelerating voltage. Scan speed refers to the velocity of the electron beam movement. Line offset represents the distance between two adjacent single tracks.

The three process parameters (beam current, scan speed, and line offset) were set using a uniform experimental design to make three types of process parameters distributed uniformly in 3D space, as shown in Fig. 1a, and the specific 32 groups of parameters are shown in Table 2. Here, the uniform experimental design [35] is one of the DoE (design of experiments), which is an experimental design method that considers only the uniform scattering of test points over the test range. It is convenient for obtaining data sets that are distributed in a high-dimensional space, allowing the data points to be distributed as uniformly as possible in the space of beam current - scan speed - line offset. Since too small / too large beam current, scan speed and line offset do not print samples stably, the beam current, scan speed and line offset vary between 2 and 40 mA, between 100 and 2000 mm/s and between 0.1 and 0.5 mm respectively, according to the EBM machine's parameter limitations and operating experience. Using these three process parameter ranges as boundaries, the JMP software (Free Trial) was used to generate a uniform distribution of 32 data points in this space. The scanning strategy for the electron beam is shown in Fig. 1b, and contour scanning is performed, and a bi-directional scanning strategy is used to build the S30C part. That is, for one layer (n), the electron beam scans on the S30C powder bed following the path shown by the blue arrow, while for the next layer (n + 1) the scanning direction of the electron beam is rotated by 90°, following the path shown by the red arrow. Fig. 1c shows an overview of the fabricated parts. The surface topography of the parts was analyzed using a Keyence® VR-3200 wide-area 3D measurement system. SEM and X-ray CT (Comscantecno Co., Ltd, Yokohama, Japan) were used to analyze the internal defects of the parts. In the analysis of defects using X-ray CT, the size of the defects was defined by the effective diameter. The effective diameter is the diameter of the sphere, which has the same volume as the defect. The absolute density of the S30C parts was measured using Archimedes' principle [36], as shown in formula (1):

$$\rho_{S30C} = \frac{m_{S30C} \bullet \rho_{water}}{m_{cS30C} - m_c} \tag{1}$$

where $\rho_{water} = 0.9982$ g/cm^3 is the density of water at 20 °C. $m_{cS30C} = m_c + m_{S30C}$, m_{S30C} are the masses of the S30C parts in the air. m_c is the sum of the mass of the container, water, and submerged part holder.

2.3. Numerical simulations

Computational thermo-fluid dynamics (CFD) is a computational method for solving the thermo-fluid dynamics equations [37,38]. In this study, we used Flow3D® [39], a commercial CFD software, to simulate the melt pool geometry, fluid motion, and temperature field for a single-track scan in the PBF-EB process. To accurately describe the

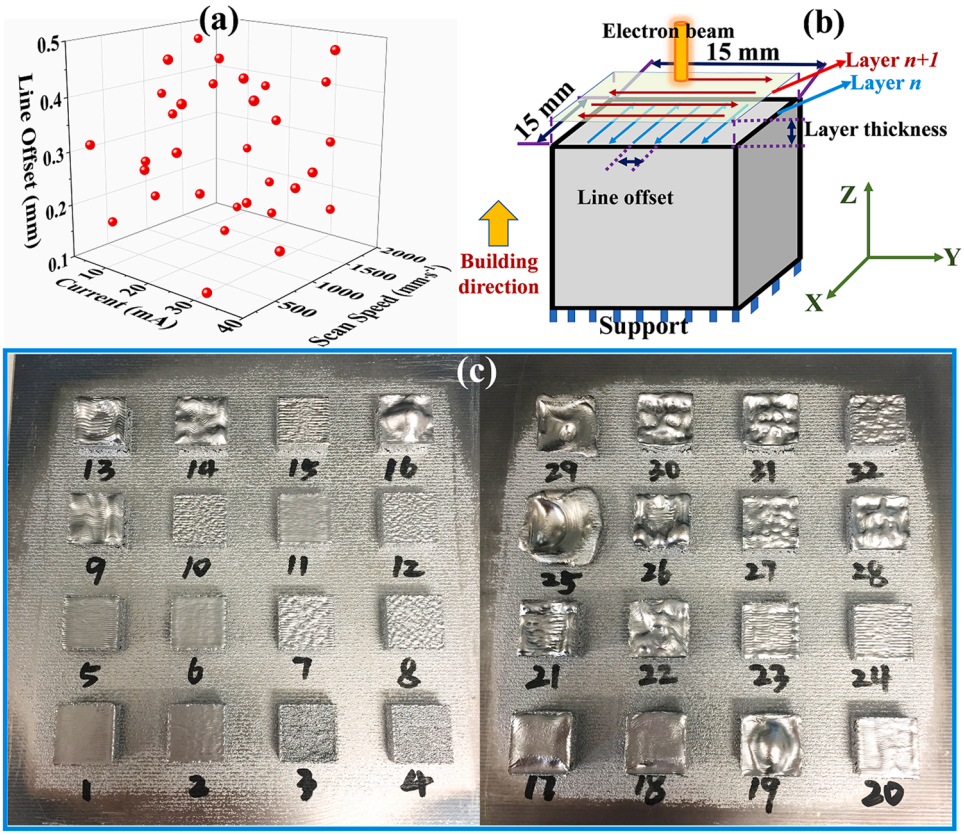

Fig. 1. (a) Process parameters of PBF-EB by a uniform experimental design. (b) Schematic of the scan strategy and part of a 15 × 15 × 4.5 mm^3 dimension fabricated by PBF-EB, and (c) overview of two batches of S30C cube parts fabricated on the SUS304 substrate.

Table 2
Process parameters for melting used herein.

Sample No.	Current / mA	Scan Speed / mm s^{-1}	Line Offset / mm	Sample No.	Current / mA	Scan Speed / mm s^{-1}	Line Offset / mm
1	6.31	138	0.32	17	25.14	247	0.42
2	3.83	480	0.15	18	22.77	312	0.33
3	2.68	1192	0.37	19	24.05	1483	0.16
4	5.05	1567	0.47	20	21.55	1606	0.21
5	8.73	663	0.27	21	28.73	779	0.45
6	7.38	845	0.19	22	27.54	906	0.22
7	9.8	958	0.35	23	26.41	1370	0.35
8	10.51	1963	0.24	24	29.92	1852	0.41
9	14.49	362	0.28	25	31.16	193	0.11
10	13.11	1313	0.4	26	34.72	537	0.43
11	12.05	1721	0.13	27	33.7	1669	0.31
12	15.69	1905	0.38	28	32.45	1795	0.17
13	19.02	424	0.48	29	39.21	600	0.18
14	20.34	723	0.23	30	35.83	1021	0.26
15	17.83	1119	0.46	31	38.21	1089	0.29
16	16.93	1250	0.12	32	37.16	1436	0.49

PBF-EB process of the S30C alloy, its physical model should be customized using specific conditions, and a "Medium_-Carbon_Steel-SCMn_2B" model in Flow3D® software was chosen. The buoyancy effect was intrinsically considered, and it was incorporated into the density as a function of temperature. In addition, three factors (Marangoni force, capillary force, and vapor recoil pressure) influence the surface state and were also incorporated in this model. A further detailed description of the model can be obtained from Refs. [40,41].

2.4. Basic idea of predicting internal defects using machine learning algorithms

In the PBF-EB process, process mapping is a typical classification problem. In this study, poor quality (with internal defects) and good quality (without internal defects) parts were classified. It should be noted that the internal defects used for classification in this study were defects introduced by unsuitable printing parameters; small spherical pores originating from entrapment in the virgin powder are not considered. Based on the X-ray CT results from the virgin powder (the data is shown in the Supplementary material, Fig. S2), it can be seen that the defect size in the virgin powder is usually less than or equal to 50 μm. The resolution of the reconstructed data of the X-ray CT, used in this study, is 50 μm, and then defects with the diameter of > 50 μm are considered for the quality classification of the parts in this study. Five machine learning techniques (logistic regression (LR), support vector machine (SVM), decision tree (DT), XGBoost, and naive Bayes (NB)) for binary classification models, which are commonly used to solve classification problems, were applied and compared. Among them, the techniques with the highest model performance were used to construct the processing maps. The five specific machine learning techniques used herein are explained in the Supplementary material.

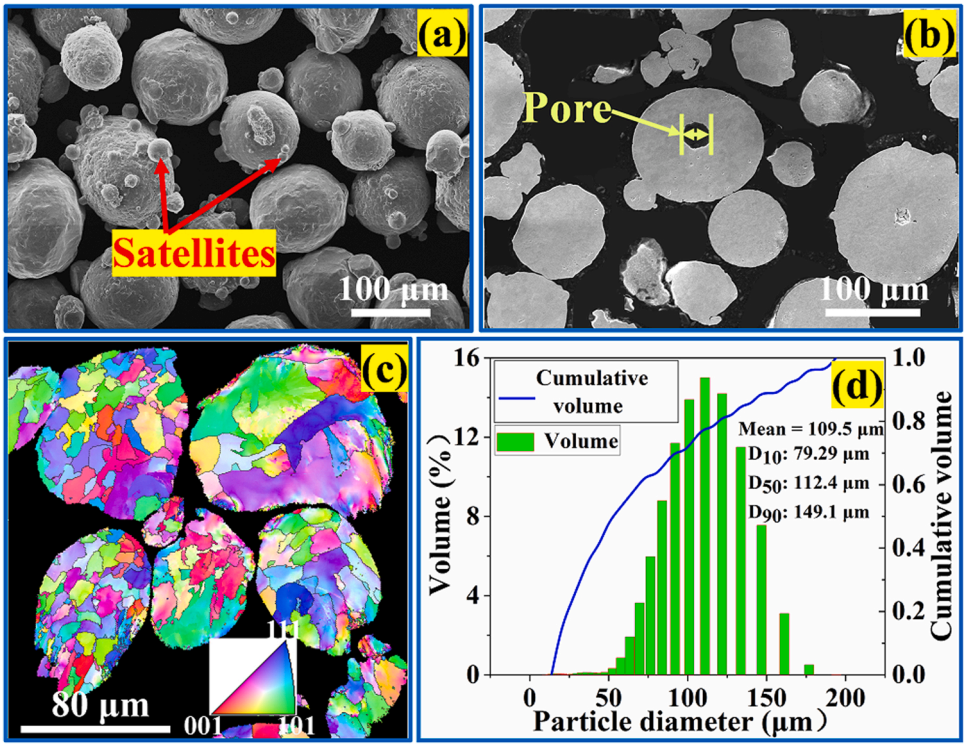

Fig. 2. Part characteristics of the gas-atomized S30C powder. (a) SEM images of the surface morphology of the powder, (b) SEM images of the cross-section of the powder, (c) IPF maps of the cross-section of the powder, and (d) particle size distribution of the powder.

3. Results and discussion

3.1. Powder characteristics of S30C alloy

Fig. 2a shows the surface morphology of the S30C powder. The powder had a relatively uniform particle size distribution and a small amount of satellite powder. Fig. 2b shows the SEM image of the cross-section of the powders, and there is an obvious pore present in the individual powder. The main reason for the formation of this pore is the encapsulation of argon in the spheroidization of the molten droplets during the atomization process [42]. The inverse polar figure (IPF) in Fig. 2c shows that each powder particle has a polycrystalline structure. As shown in Fig. 2d, the particle size of the S30C powder ranged from 50 to 160 μm, with an average size of 109.5 μm. In terms of sizes, 10% of powders are less than 79.29 μm, 50% are less than 112.4 μm, and 90% are less than 149.1 μm. In summary, this S30C alloy powder has high purity and a narrow particle size distribution and is considered suitable for PBF-EB.

3.2. Effect of processing parameters on surface morphology

Fig. 3 shows the surface morphology of the parts observed with the digital microscope, which can be classified into porous, even, and uneven. The surface quality is usually related to the energy input. The input energy is often expressed in terms of the global energy density E_{volume} ($E_{volume} = P/(V_{scan}L_{offset}Z_{layer})$) (J/mm^3) [21], and the results of the calculation are listed in Table 3. P is the power, $P = U$ (accelerating voltage) $\times$ I (beam current). V_{scan}, L_{offset}, and Z_{layer} are the scan speed, line offset, and layer thickness, respectively. The E_{volume} increases from part 3 (4.86 J/mm^3) to part 25 (1174.19 J/mm^3), and the surface of parts 25 and 29 with highest energy density exhibits severe unevenness owing to the excessive energy input. As shown in Fig. 3 and Table 3, some samples with different $E_{volumes}$ show different surface morphologies, but E_{volume} does not always determine the surface morphology. For example, parts 1, 2, 5, 6, and 11 are even surfaces, but E_{volume} is divided into two regions.

Table 3
Global energy density and surface morphology of different parts.

Sample No.	Global Energy Density / J mm^{-3}	Surface Morphology	Sample No.	Global Energy Density / J mm^{-3}	Surface Morphology
1	114.31	Even	17	193.87	Uneven
2	42.56	Even	18	176.92	Uneven
3	4.86	Porous	19	81.09	Uneven
4	5.49	Porous	20	51.12	Uneven
5	39.01	Even	21	65.57	Uneven
6	36.77	Even	22	110.54	Uneven
7	23.38	Porous	23	44.06	Uneven
8	17.85	Porous	24	31.52	Porous
9	114.36	Uneven	25	1174.19	Uneven
10	19.97	Porous	26	120.29	Uneven
11	43.09	Even	27	52.11	Uneven
12	17.34	Porous	28	85.07	Uneven
13	74.76	Uneven	29	290.44	Uneven
14	97.85	Uneven	30	107.98	Uneven
15	27.71	Porous	31	96.79	Uneven
16	90.29	Uneven	32	42.25	Uneven

Fig. 4a shows the surface morphology corresponding to the parts with different $E_{volumes}$, some of which (e.g., parts 1 and 32) are not completely distinguished according to E_{volume}. This demonstrates that the energy input does not depend on E_{volume}. If E_{volume} is a characteristic parameter that reflects the input energy for melting powder, the surface morphology would monotonously depend on E_{volume}. This fact indicates that E_{volume} is not a characteristic parameter for the energy input to the built parts. The global energy density E_{volume} has no physical meaning, and in this study, it was used to reduce the dimension in Fig. 4b. As shown in Fig. 4b, the three types of surface morphologies are divided into three regions: porous surface, even surface, and uneven surface.

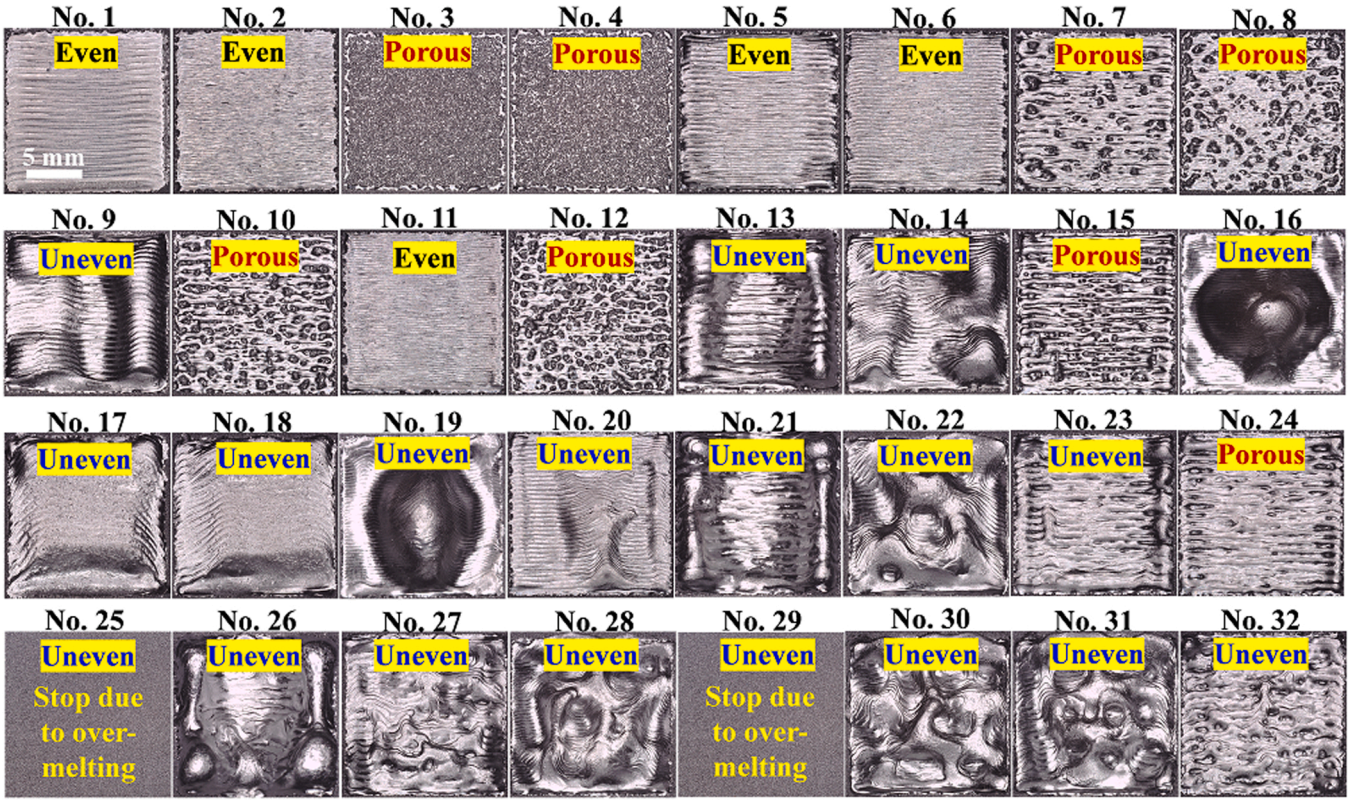

Fig. 3. Digital images of the surface morphology of S30C parts built by PBF-EB with different process parameters.

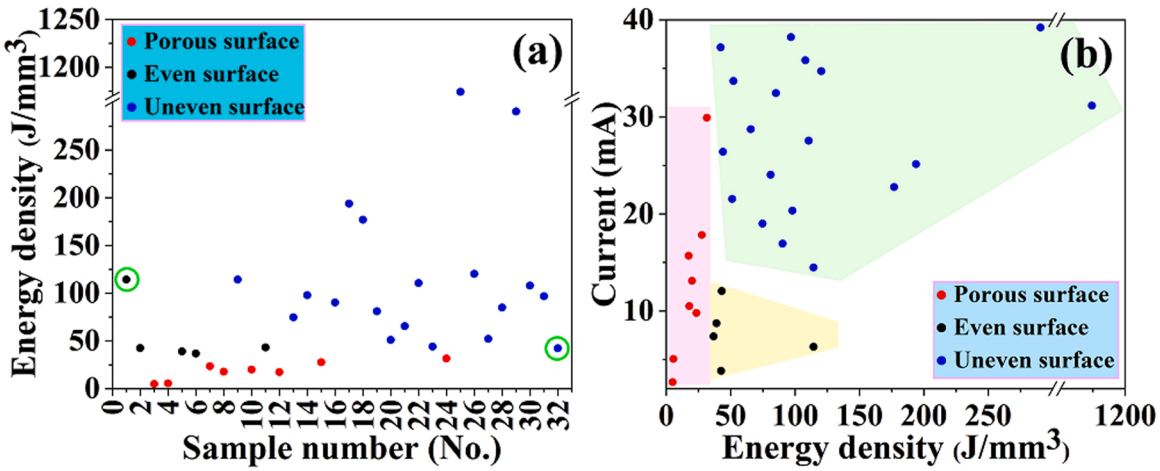

Fig. 4. (a) Scatter plot of energy density and surface morphology corresponding to different parts, and (b) scatter plot of energy density, current, and surface topography corresponding to different parts.

When I is too high, it tends to lead to excessive energy input, regardless of E_{volume}.

Fig. 5 shows the 3D surface morphology of the outermost surface of the parts. Surface flatness is usually used to characterize the surface morphology of parts quantitatively, and we introduced two parameters of surface flatness [43,44]: the commonly used Sa (arithmetic mean height) and Sdr (developed interface area ratio). Where Sa is a parameter of surface expansion in terms of Ra (arithmetic mean height of the line), representing the average of the absolute value of the difference in height of each point with respect to the mean height, and is expressed as follows [44]:

$$Sa = \frac{1}{A}\iint_A |Z(x,y)|dxdy \tag{2}$$

Sdr is the expanded area (surface area) of the defined area, indicating the amount of area added relative to the defined area. The Sdr of a perfectly flat surface is 0. If the surface has a slope, Sdr increases. The expression [44] is as follows:

$$Sdr = \frac{1}{A}\left[\iint_A \left(\sqrt{\left[1+\left(\frac{\partial z(x,y)}{\partial x}\right)^2+\left(\frac{\partial z(x,y)}{\partial y}\right)^2\right]}-1\right)dxdy\right] \tag{3}$$

Here, A is the area of the measurement target area, and $|Z_{(x,y)}|$ is the absolute value between the height of the measurement mean plane and that of the convex part or the depth of the concave part. Fig. 6 shows the surface flatness, Sa, and Sdr, of the built parts, and the values are listed in Table 4. The three types of surface morphology—porous, even, and uneven—are indicated by red, black, and blue dots, respectively. The results show that Sa can distinguish uneven surfaces, but Sa cannot distinguish porous surfaces. The surfaces of parts 3 and 4 are porous, but

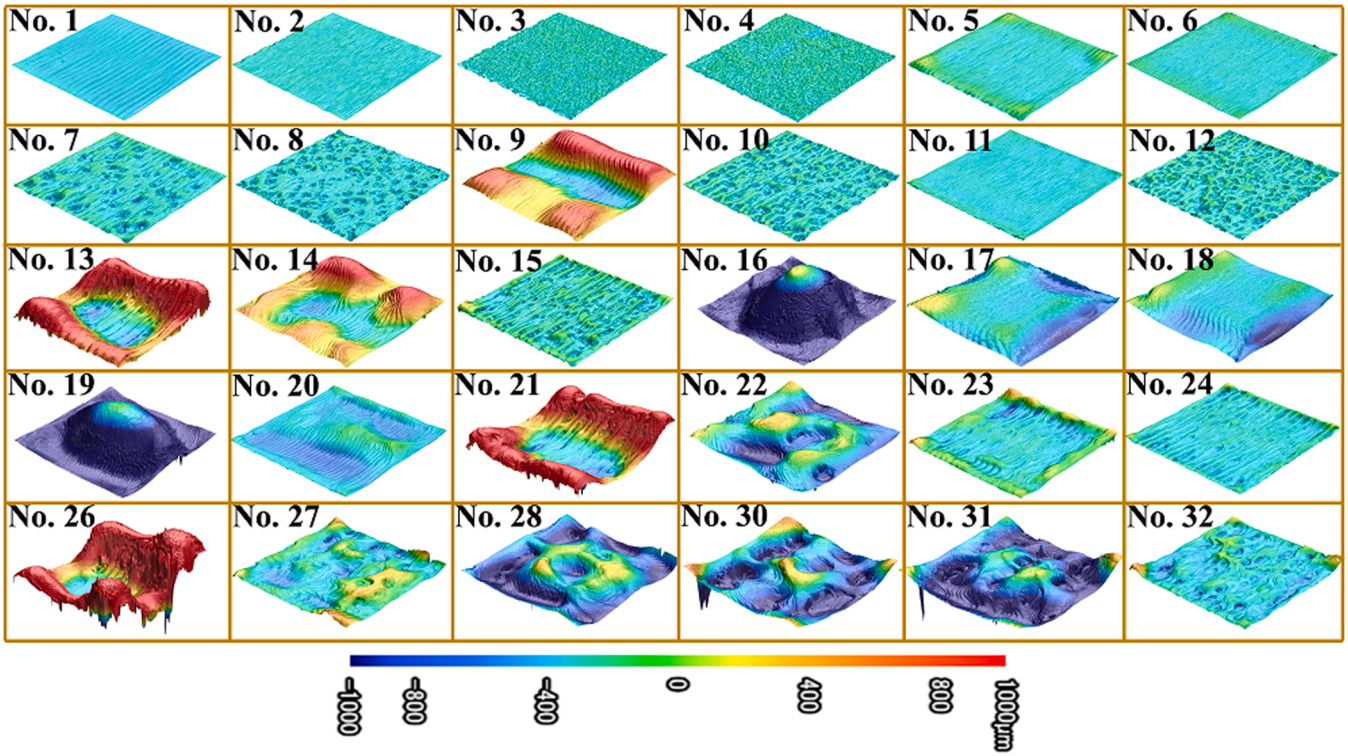

Fig. 5. Three-dimensional surface topographical images of built parts.

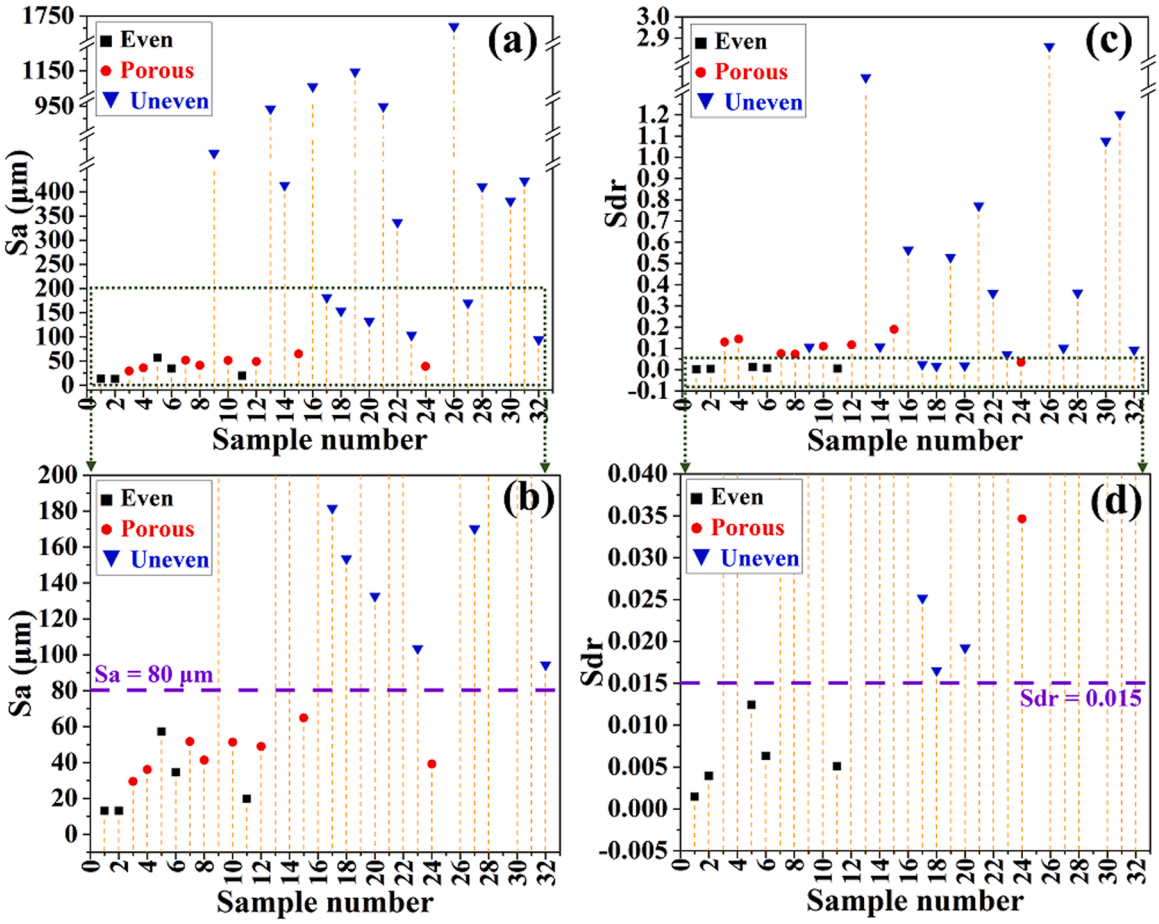

Fig. 6. Sa and Sdr values and corresponding surface quality of the built parts in Fig. 5. (a) The values of Sa, (b) partial enlarged view of (a), (c) the values of Sdr, and (d) partial enlarged view of (c).

Table 4
Values of Sa and Sdr of the built parts. Each part was divided into two classes and labels according to the value of Sdr (when Sdr < 0.015, it is "good" and when Sdr ≥ 0.015, it is "bad"). Parts with even surface are defined as "good" and labeled as 1. Parts with uneven and porous surfaces are defined as "bad" and labeled as 0.

Sample No.	Sa / μm	Sdr	Class	Label	Sample No.	Sa / μm	Sdr	Class	Label
1	13.133	0.00146	Good	1	17	181.638	0.02516	bad	0
2	13.094	0.00394	Good	1	18	153.476	0.01653	bad	0
3	29.485	0.13052	Bad	0	19	1148.212	0.52964	bad	0
4	36.079	0.14411	Bad	0	20	132.629	0.01923	bad	0
5	57.297	0.01245	Good	1	21	949.564	0.77157	bad	0
6	34.543	0.00634	Good	1	22	337.058	0.35956	bad	0
7	51.669	0.07524	Bad	0	23	103.607	0.07185	bad	0
8	41.345	0.07288	Bad	0	24	39.174	0.03462	bad	0
9	516.389	0.10708	Bad	0	25	–	–	bad	0
10	51.353	0.10994	Bad	0	26	1728.235	2.86081	bad	0
11	19.783	0.00512	Good	1	27	170.217	0.10187	bad	0
12	48.907	0.11759	Bad	0	28	411.305	0.3616	bad	0
13	944.751	2.24503	Bad	0	29	–	–	bad	0
14	413.693	0.10804	Bad	0	30	380.927	1.07691	bad	0
15	64.834	0.18965	Bad	0	31	422.997	1.20152	bad	0
16	1117.634	0.56409	Bad	0	32	94.452	0.09391	bad	0

the Sa of the parts is smaller than that of part 5 with an even surface. On the contrary, Sdr can distinguish even surfaces from porous or uneven surfaces. In addition, for the S30C alloy fabricated by PBF-EB, we can obtain the quantitative criteria that classify the surface morphology. That is, the surface is even when Sdr < 0.015, uneven when Sa ≥ 80 μm, and porous when Sdr ≥ 0.015 and Sa < 80 μm. These quantitative criteria can not only classify the three types of surface morphology but also can be used to classify surfaces as bad or good for subsequent machine learning techniques to predict the range of process parameters of parts with even surfaces.

3.3. *Effect of process parameters on internal defects and density*

To reveal the relations between internal defects and surface morphology, cross-sectional microstructures of the built parts parallel to the building direction were observed using SEM, as shown in Fig. 7. No internal defects were observed in the parts with even surfaces, indicating that the part was of good quality. In contrast, the parts with porous

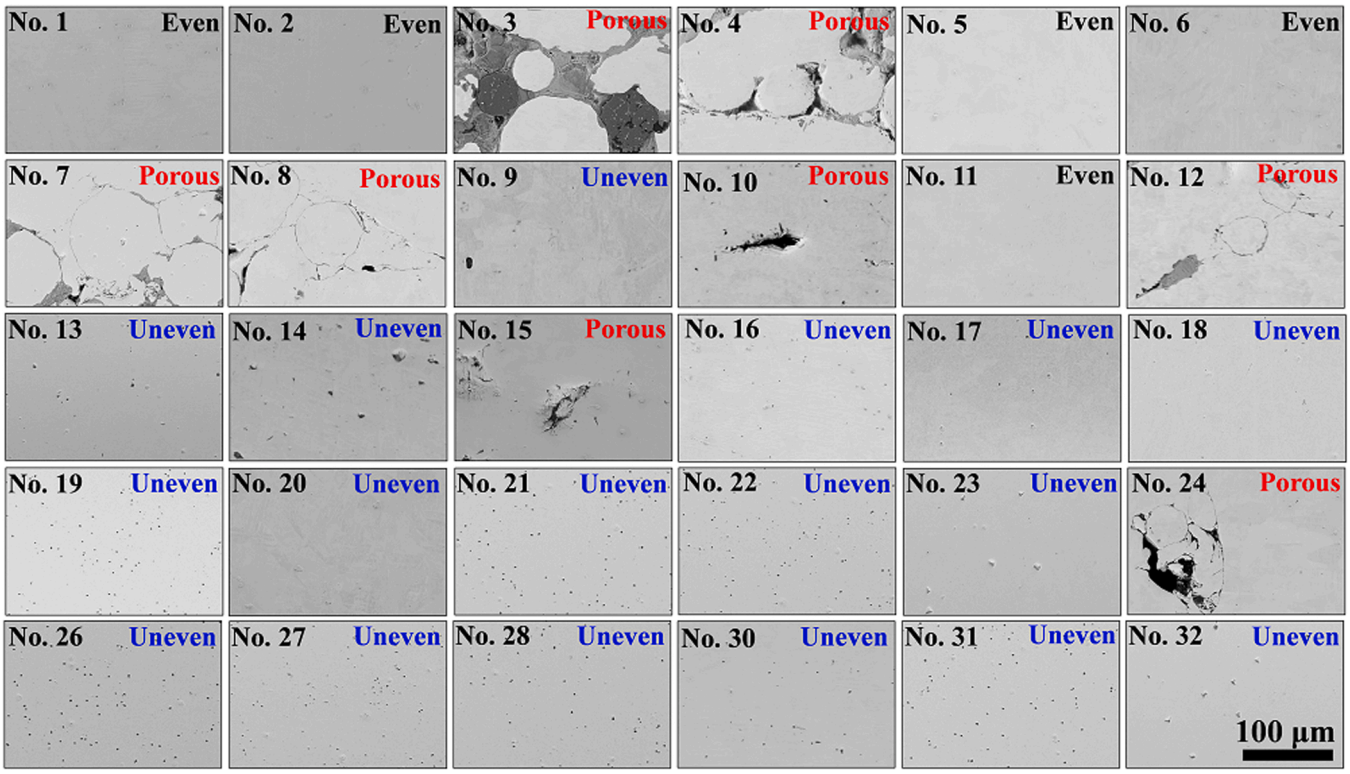

Fig. 7. Cross-sectional SEM images parallel to the building direction of S30C built parts. A comparison with Figs. 3 and 5 reveals that surface morphology correlates with internal defects.

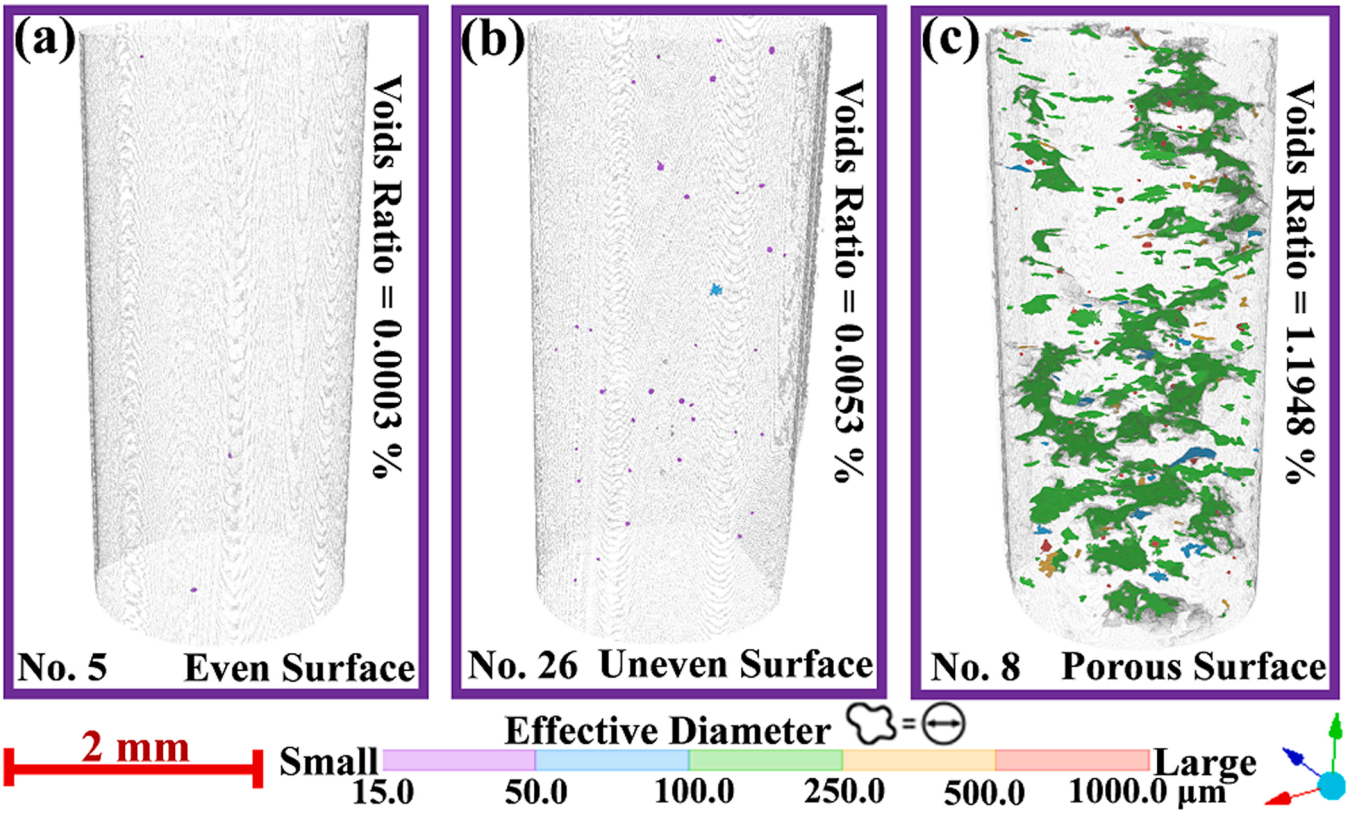

Fig. 8. Three-dimensional rendering of X-ray CT analysis of (a) part 5 with even surface, (b) part 26 with uneven surface, and (c) part 8 with porous surface. The internal defects are marked with different colors according to their effective diameter.

surfaces contain many large-size defects, that is, unmelted powder (e.g., parts 3, 4, 7, among others) or irregularly shaped pores (e.g., parts 10 and 15). These large defects are the lack of fusion-type defects caused by insufficient energy, which act as a starting point for cracking during the service life of the part and greatly deteriorates its overall performance. In contrast, parts with uneven surfaces contain many spherical pores that also deteriorate the overall performance.

The relations between internal defects and surface morphology were further analyzed by X-ray CT, and the results are shown in Fig. 8. Fig. 8a, b, and c are the results of part 5 with even surface, part 26 with uneven surface, and part 8 with porous surface, respectively. Part 5, with an even surface, contains few defects with a void ratio of only 0.0003%, and part 26 with an uneven surface contains many spherical pores less than 100 μm in size with a void ratio of 0.0053%, while part 8 with a porous surface contains a large number of large irregularly shaped defects with a void ratio of 1.1948%.

The defects were also classified according to the shape of the defects from the X-ray CT results, as shown in Fig. 9. In Fig. 9, red represents spherical shape defects, orange represents elongated shape defects, blue represents flat shape defects, and green represents other irregular shape defects. Part 5 is defect-free, and part 26 contains only spherical defects. Part 8 contains not only red spherical defects (Fig. 9c-1) but also many irregularly shaped defects. Fig. 9d shows the volume fraction of defects in part 8 as a function of the defect shape. The volume fractions of the spherical defects, elongated shape defects, flat shape defects, and other irregularly shaped defects were 1.42%, 1.21%, 2.71%, and 94.66%, respectively.

The measured densities of the parts are shown in Fig. 10. To evaluate errors induced during measurement and calculation of densities, each sample was measured five times and its average value was calculated, while we also indicated its standard deviation with an error bar, and the results are shown in Fig. 10a. The standard deviation in Fig. 10a is larger for porous and uneven samples and smaller for even samples. The porous and uneven samples have rough surface and opened pores on the surface. In the measurement of these samples, water may get into the opened pores, and amount of water in the opened pore is not constant for each measurement. This is the reason of large standard deviation in the porous and uneven samples. Fig. 10a also shows that the density is clearly divided into three classes according to the three different surface morphologies: $\rho_{even} > \rho_{uneven} > \rho_{porous}$, and the absolute density of the five even surface parts is more than 7.7683 g/cm^3 and the highest is 7.7962 g/cm^3 of part 1. Here, the relative densities of the parts were calculated based on the density of the rolled S30C alloy (7.838 g/cm^3) from the equation $\left(\frac{\rho_{S30C}}{7.838}\right) \times 100\%$ as shown in Fig. 10b. Fig. 10b shows that the relative densities of the parts with even surfaces are greater than 99.11%. The relative density of part 1 with an even surface shows the highest value of 99.46%, while that of part 3 with a porous surface shows the lowest value of 66.25%. This indicates that the density and internal void ratio of the part are highly correlated.

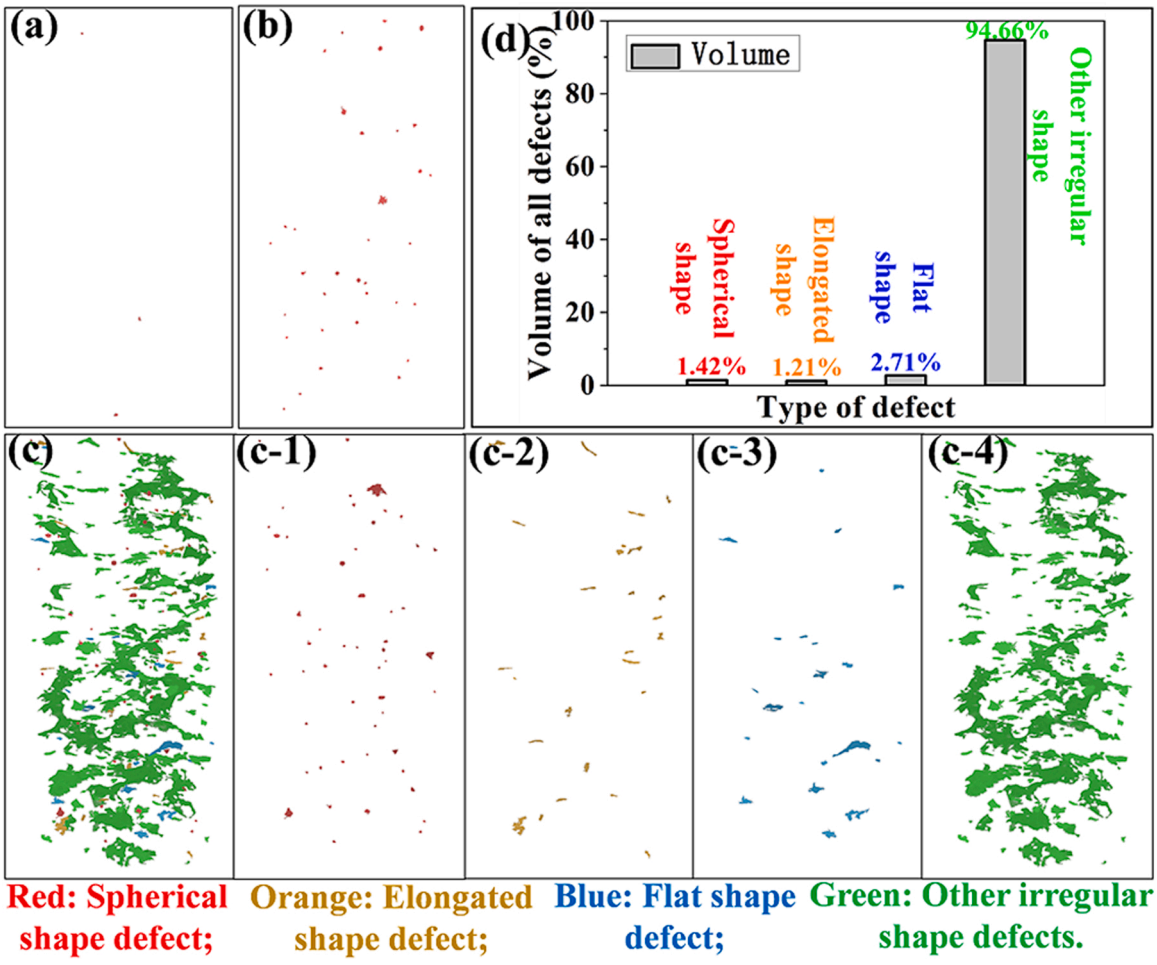

Fig. 9. Three-dimensional rendering of X-ray CT results as a function of the shape of defects. (a) Part 5 with even surface indicating free of internal defects, (b) part 26 with uneven surface indicating spherical shape defects, and (c) the part 8 with porous surface indicating several irregularly shaped defects. (c-1), (c-2) (c-3), and (c-4) show the separated figure with spherical shape defects, elongated shape defects, flat shape defects, and other shape defects, respectively, and (d) the volume fraction of defects in part 8 with a porous surface as a function of the shape of defects.

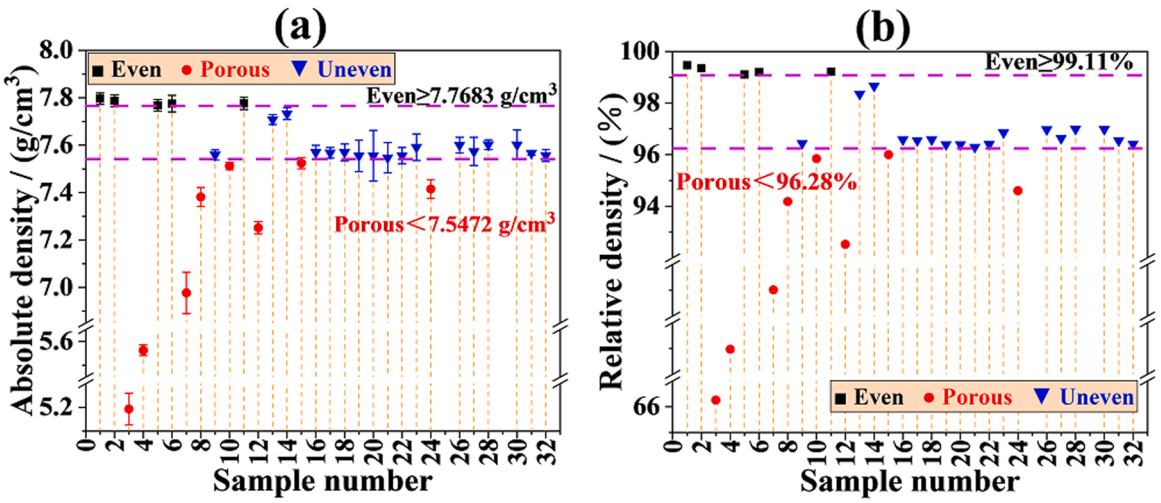

Fig. 10. Variation of the density of corresponding surface quality of S30C parts at different process parameters: (a) absolute density and (b) relative density.

3.4. Effects of processing parameters on surface flatness and internal defects generation mechanisms of PBF-EB parts

One of the goals of PBF-EB technology is to manufacture high-density parts. Owing to the complex solidification process of PBF-EB, various defects appear in parts that reduce the mechanical properties of PBF-EB parts and affect their safety in use. In this paper, we assume that the defects can be detected from the surface morphology. The above experimental results indicate that this assumption is valid for PBF-EB built parts. In order to confirm the validness of the assumption, we conducted simulation and investigated the mechanisms by which processing parameters affect the surface morphology and internal defects of parts. Different processing parameters result in different energy inputs, which in turn affect the melt pool size, melt pool shape, solidification rate, and temperature gradient, and consequently affect the surface morphology and internal structure [1,28,40,41]. In the simulation of the PBF-EB process, the heat source (q) must be described as the energy input by the electron beam, which is usually described as having an approximate Gaussian distribution as follows [40]:

$$q(r) = \frac{2\eta Q}{\pi r_0^2} exp\left(-\frac{2r^2}{r_0^2}\right) \tag{4}$$

where r_0, Q, r, and η are the effective beam radius, beam power, actual spot radius, and energy efficiency of the energy density decaying to $1/e^2$ at the center of the beam spot, respectively. Multi-scale physical coupling effects occur in the melt zone, including the interaction between the solid, liquid, and gas phases, as well as the Marangoni effect, electron impact pressure, and vapor recoil pressure. This study focused mainly on the behavior of the melt pool, and we simulated three cases of

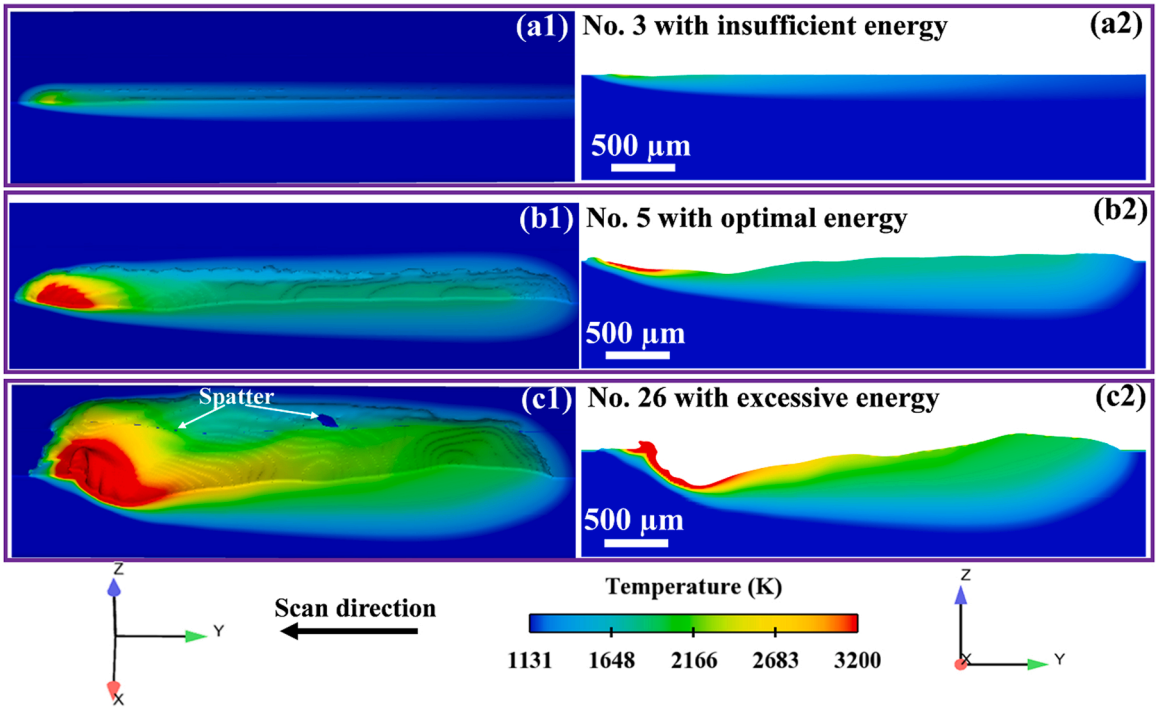

Fig. 11. Temperature distribution in the melt pool simulated by CFD. (a1) (a2) the condition of the part 3 with insufficient energy input, (b1) (b2) the condition of the part 5 with optimal energy input, (c1) (c2) the condition of the part 26 with excessive energy input. (a1)–(c1) are the 3D images of half symmetry models, and (a2)–(c2) are the y-z cross-sectional planes.

single-track melting without powder. The three cases are the condition of part 3 with a porous surface including irregular shape defects, the condition of part 5 with an even surface including no internal defects, and the condition of part 26 with uneven surface including spherical shape defects.

Figs. 11 and 12 show the temperature field and the solid fraction of the melt pool for the three cases, respectively, where a, b, and c are figures corresponding to low energy input (Part 3), medium energy input (Part 5), and high-energy input (Part 26), respectively. Figs. 11 and 12 show that when the energy input is too small, the melt pool is small and shallow (the melt pool depths for low, medium, and high energy inputs are 0.25 mm, 0.79 mm and 2.37 mm respectively, as measured by Fig. 12c1-c2), and the maximum temperature in the melt pool is very low, leading to unmelted powder and interlayer lack of fusion during the PBF-EB process. On the contrary, when the energy input is too high, the melt pool is very large and deep with a severely wavy surface and spattering, and the maximum temperature in the melt pool is very high. Fig. 13 shows that before the formation of a spatter, the melt pool is extremely unstable owing to excessive energy, and a convex prominence is formed at the front of the pool (Fig. 13a). The intense dynamic flow due to the high thermal gradient generates a convex prominence toward the oblique upper part of the melt. When the liquid at the edge of the depression has sufficient kinetic energy, a liquid droplet spatters from the melt pool surface (Fig. 13b). This spattering at very high temperatures results from the ejection of liquid metal droplets from the melt pool. In contrast, when the energy input was appropriate, the melt pool was stable (Figs. 11b2 and 12b2).

Fig. 14 shows the melt flow direction and velocity in the x-z cross-sectional plane for the three conditions corresponding to Fig. 11. The backward liquid flow from the hot spot has a higher flow rate in the case of high-energy input than in the case of low-energy input. This is caused by the large thermal gradient in the case of high-energy input. The main driving force for the liquid flow is the Marangoni force, i.e., the surface tension caused by the temperature gradient, which carries the melt from the hot spot to the tail of the melt pool. The Marangoni effect is expressed as follows [40,41]:

$$\gamma(T) = \gamma_L + \frac{d\gamma}{dT}(T - T_L) \tag{5}$$

Where, γ is the surface tension, T is the temperature of melt pool. γ_L and T_L are the surface tension and temperature at the liquidus, respectively. $\frac{d\gamma}{dT}$ is the temperature coefficient of the surface tension. The Marangoni force along the tangent of the surface ($\frac{d\gamma}{dx}$) can be expressed as [40,41]:

$$\frac{d\gamma}{dx} = \frac{d\gamma}{dT}\nabla T \tag{6}$$

Here, ∇T is the temperature gradient at the liquid–gas interface. The higher the input energy, the higher the temperature T at the melt pool depression location (Fig. 11) and the higher the temperature gradient ∇T, i.e., the higher the Marangoni force according to Eqs. (5) and (6). Excessively high Marangoni forces lead to a violent flow of the melt that does not spread uniformly along the surface of the melt pool but tends to form bumps in parts with high surface tension [41]. In addition, the vapor recoil pressure (P_{recoil}) is also considered as another driving force for the melt pool flow, which is a normal reaction force caused by the interaction of the metal vapor with the atmosphere and can be written as [40,41]:

$$P_{recoil}(T) = Ap_0 exp\left[\frac{\Delta H_{LV}(T - T_V)}{RTT_V}\right] \tag{7}$$

where p_0 is the atmospheric pressure (Pa), ΔH_{LV} is the latent heat of vaporization, T is the temperature of melt pool, T_V is the vapor saturation temperature (boiling temperature), R is the gas constant, and A is the ratio coefficient. For a high-energy input, a higher T produces a larger P_{recoil}. These phenomena may lead to the formation of pores in the melt pool that are usually spherical or elliptical in shape owing to the dominant surface tension of the liquid metal [45,46].

The distribution of defects within the low-energy input (Part 3), suitable energy input (Part 5), and high-energy input (Part 26) parts were examined by SEM, and the results are shown in Fig. 15a, b, and c, respectively. Fig. 15a demonstrates that the defect contains unmelted powder, indicating that the irregular-shaped defect in part 3 is mainly caused by the unmelted powder due to the lack of fusion. Fig. 15b reveals the uniform internal structure of part 5 with an even surface printed at suitable energy input conditions, with no defects present. However, there are many spherical pores with excessively high energy inputs in part 26, as shown in Fig. 15c. These spherical pores may be associated with metal vapor due to overheating and unstable melt pools, as well as argon entrapped during the manufacture of gas-atomized S30C powders [25,45–49].

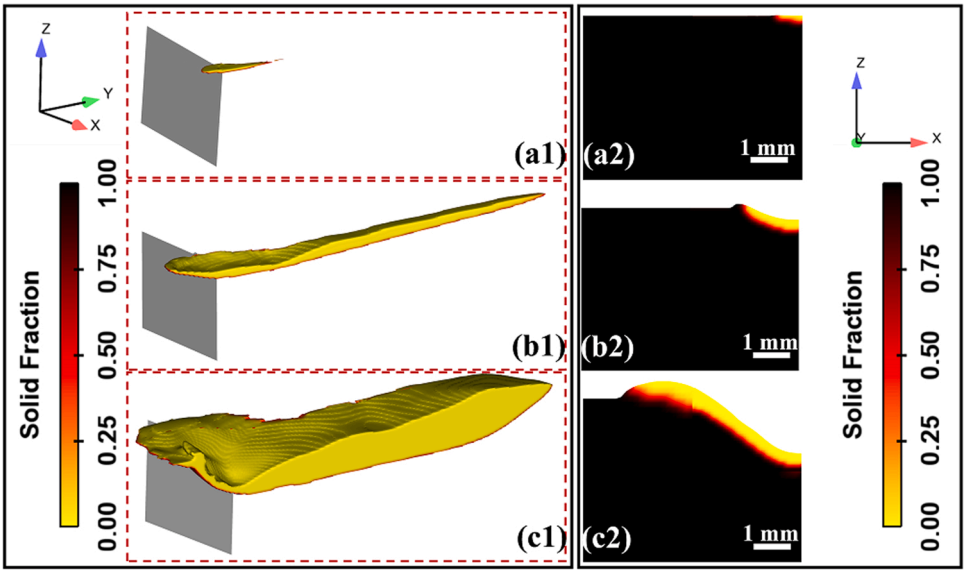

Fig. 12. Solid fraction in the melt pool simulated by CFD. (a1) (a2) the condition of the part 3 with insufficient energy input, (b1) (b2) the condition of the part 5 with optimal energy input, (c1) (c2) the condition of the part 26 with excessive energy input. (a1)–(c1) Three-dimensional images of half symmetry models, and (a2)–(c2) the x-z cross-sectional planes of the melt pool at the position of the planes shown as a gray plane in (a1)–(c1).

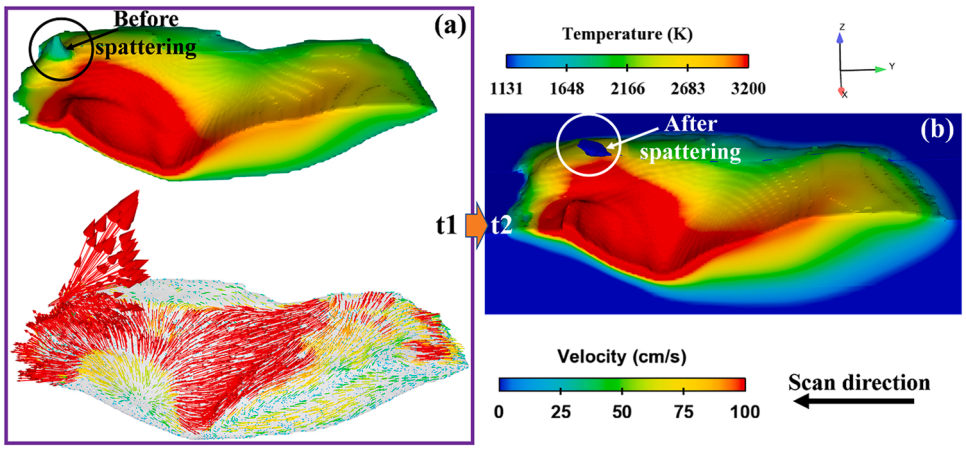

Fig. 13. Simulation results of the spatter formation process. (a) Temperature distribution and flow velocity in the melt pool before the spatter formation. (b) Temperature distribution of the melt pool after the spatter formation.

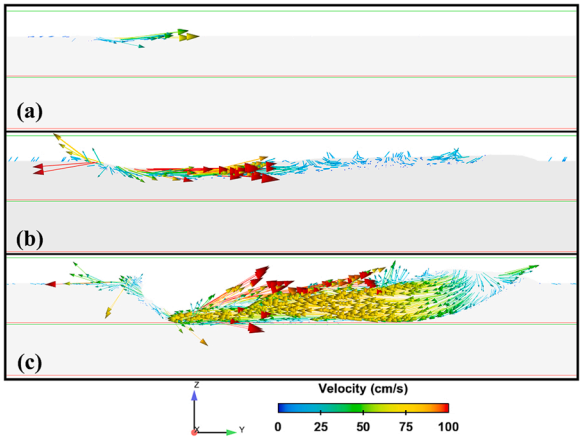

Fig. 14. Liquid flow corresponds to the conditions in Fig. 11(a2)–(c2).

In summary, the formation mechanism of the surface flatness and internal defects of the S30C alloy under different processing parameters in the PBF-EB process is clearly revealed, and a schematic is shown in Fig. 16. When the energy input is excessively high, the melt pool has a long lifetime, and a large amount of liquid phase is produced. The temperature at the melt pool tail was lower, but the temperature near the electron beam was higher, resulting in a larger temperature gradient. Therefore, the combination of the Marangoni effect, vapor recoil pressure, and electron beam agitation results in liquid flow with high velocity, and bumps are easily formed. During the subsequent layer-by-layer melting of the powder, surface bumps accumulate and eventually form surface bulges or bumps. During the melting of the pre-alloyed powder, the rapid increase in the melt pool temperature can cause Fe and Mn to evaporate easily in the melt pool. In addition, gas bubbles trapped in the atomized powder were retained in the part. These are the main reasons for the presence of a large number of spherical pores in the uneven surface parts. When the energy input was too low, insufficient fusion defects formed between the layers, and some powder was not completely melted. This is because when the energy input is low, the melt pool depth is too small to penetrate the thickness of the powder

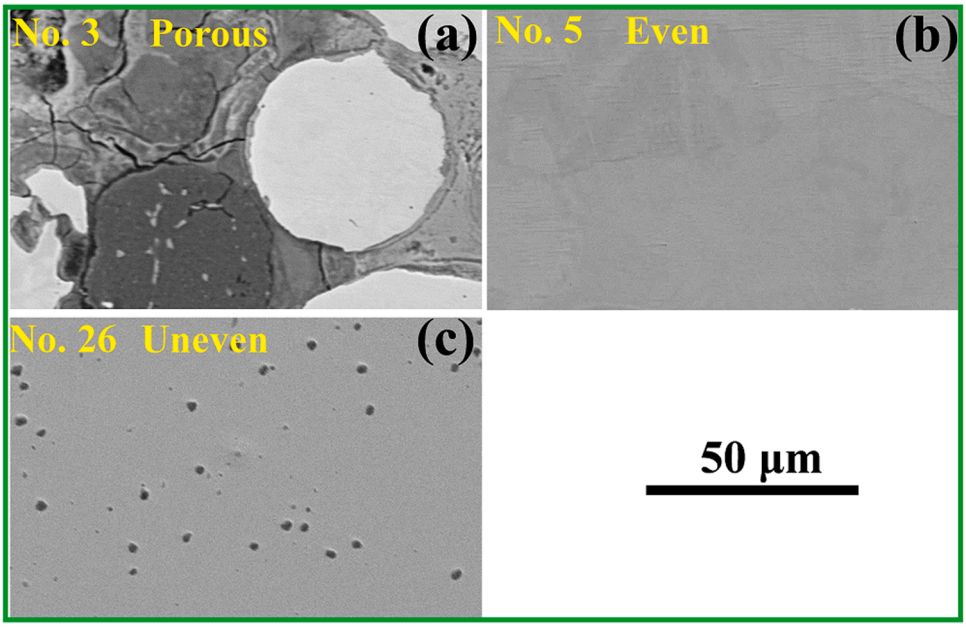

Fig. 15. Enlarged SEM microstructure images are shown for (a) porous (part 3), (b) even (part 5), and (c) uneven (part 26) of Fig. 7.

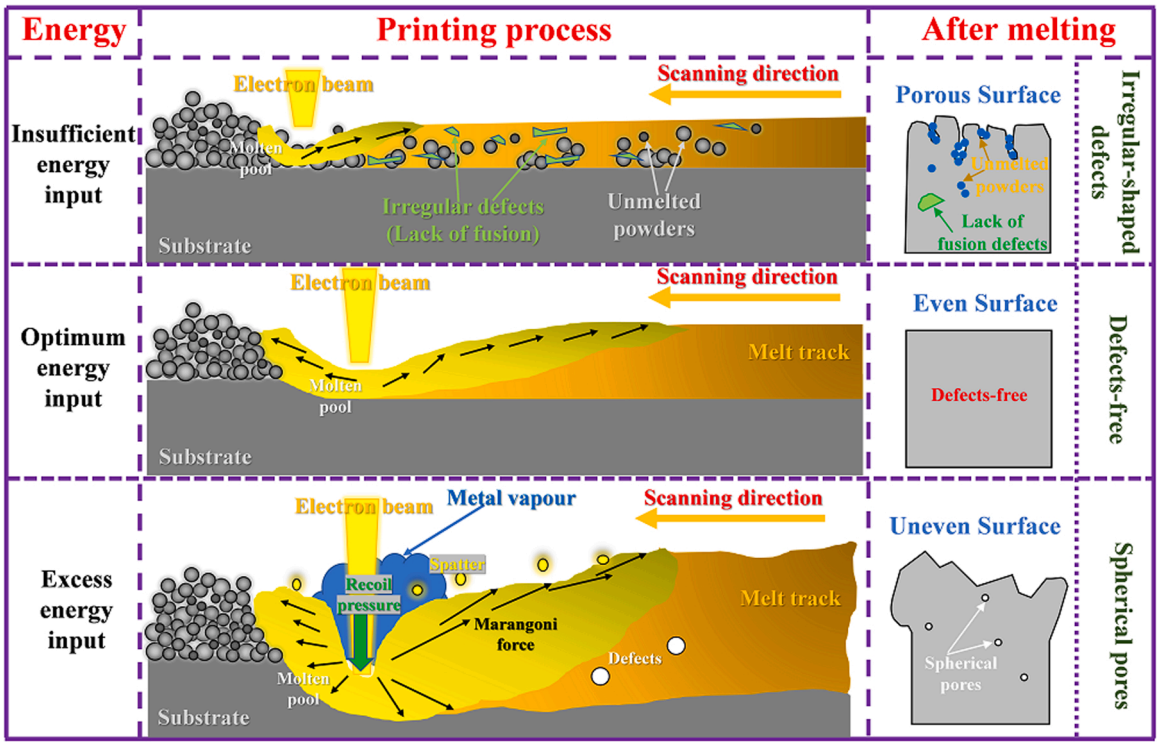

Fig. 16. Schematic of the relation between the surface morphology and internal defects, and the defects formation mechanisms for S30C alloys depending on energy input during the PBF-EB process. Optimum energy input shows defect-free even surface, excessive energy input shows uneven surface with spherical pores, and insufficient energy input shows porous surface with unmelted powders and irregular-shaped defects.

layer and cause the bottom part of the powder layer to be fully melted.

3.5. Development of a new framework to accelerate the fabrication of PBF-EB parts without internal defects by machine learning techniques

3.5.1. Evaluation of candidate machine learning algorithms applied to the construction of the new framework

The quantitative criteria for determining the three types of surface morphologies using the Sa and Sdr values were obtained in Section 3.2. Sections 3.3 and 3.4 show that the three surface morphologies correspond to the three types of internal defects, that is, the Sa and Sdr values can be used as the criteria for determining the type of internal defects. This finding makes it feasible to easily determine the internal defects of a part via non-destructive surface flatness evaluation. In industrial applications, obtaining the process parameters for parts without internal defects is important. Among the quantitative criteria we obtained, the Sdr value can distinguish defect-free parts (corresponding to an even surface), that is, the parts have no internal defects when Sdr < 0.015. Therefore, by combining this quantitative criterion, we propose a machine learning framework to quickly predict the multidimensional processing window of parts without internal defects. Based on the magnitude of Sdr, the parts can be classified into two categories: good (without internal defects) or bad (with internal defects). The parts with Sdr < 0.015 were "good" and labeled as "1", and the parts with Sdr ≥ 0.015 were "bad" and labeled as "0", as shown in Table 4. Five machine learning techniques for classification problems (LR, SVM, DT, XGBoost, and NB) were selected for model testing and evaluation of this classification problem. The input dataset for machine learning model contains only three feature values (processing parameters: beam current, scan speed, and line offset) and the corresponding labels (0 or 1), as shown in Tables 2 and 4. When dividing the training and test sets, K-fold cross-validation was used in order to ensure that every sub-sample participated in the training and was tested, and to reduce the generalization error. That is, a dataset was divided into K copies, one of which was used for validation and the remaining K-1 copies were used for training. In the scikit-learn library of python, n_splits, shuffle and random_state are the three important parameters for K-fold cross-validation. The parameter n_splits is K. Its value is equal to the number of copies into which the data set will be divided. Shuffle is also a function that means to break up the order, if shuffle = True, then it means that the order will be shuffled and then allocated. Many functions have a random_state parameter, which is the equivalent of a random seed here, and is intended to be reproducible, and is generally used in conjunction with shuffle, which only makes sense when shuffle = True. To ensure fairness in evaluating the five machine learning models, the same parameters for K-fold cross-validation were used, i.e.: n_splits = 5, shuffle = True, random_state = 100. Commonly used metrics for evaluating the performance of a binary classifier are accuracy, precision, recall, and F1-score as shown below [50]:

$$Accuracy = \frac{TP + TN}{TP + TN + FP + FN} \tag{8}$$

$$Precision = \frac{TP}{TP + FP} \tag{9}$$

$$Recall = \frac{TP}{TP + FN} \tag{10}$$

$$F1 - score = \frac{2 \times Precision \times Recall}{Precision + Recall} \tag{11}$$

where P and N denote the total number of positive and negative observations, respectively. TP, TN, FP, and FN represent true positive, true negative, false positive, and false negative identification, respectively. The results of accuracy, precision, recall, and F1-score for the five classification models are presented in Fig. 17. The LR, DT and NB classification models were built using the algorithm library in the scikit-learn package. Test accuracy of LR, DT and NB are 0.757, 0.814 and 0.675. An XGBoost model was trained with the following important

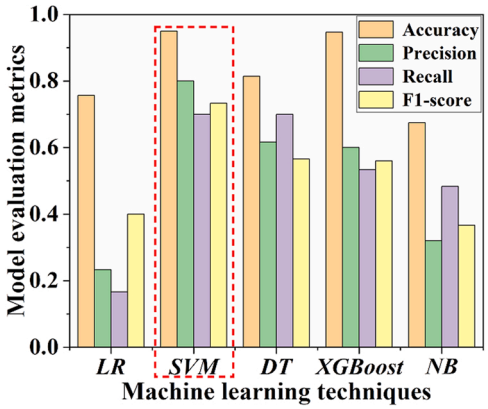

Fig. 17. Model evaluation metrics (accuracy, precision, recall, and F1-score) of the five machine learning models (LR, SVM, DT, XGBoost, and NB).

hyper-parameters in the scikit-learn library: max_depth = 6, colsample_bytree = 0.8, subsample = 0.8, learning_rate = 0.1, and it has a higher test accuracy = 0.946. Here, max_depth is the maximum depth of the tree; colsample_bytree determines the proportion of subsamples at each node division; subsample is the proportion of the samples used to fit individual base learners; learning_rate is the learning rate. The SVM classification model with radial basis function (RBF) was built using the SVM library in the scikit-learn package. The RBF was chosen to transform the feature vectors with the important parameters to be optimized being the hyper-parameter (γ) as well as the cost parameter (C). Optimizing these two parameters can help improve the performance of the SVM. GridSearchCV (grid search procedure) was used to optimize the parameters, and the final choice was: $C = 1.1$, $\gamma = 0.3$. Among all models, SVM showed the highest test accuracy of 0.950, precision of 0.80, recall of 0.70, and F1-score of 0.733, indicating that the SVM model is the most suitable for the prediction of this classification problem. It should be noted that none of these machine learning models achieve metrics of 1.0, and even some of these evaluation metrics have poor performance. However, this does not mean that machine learning models are not applicable. Fig. 17 focuses primarily on filtering the machine learning algorithm that is most applicable to this study among several commonly used models to further optimize the building parameters.

3.5.2. The new framework of process parameters – surface flatness – building quality for PBF-EB parts constructed by SVM

In the above context, this study establishes an important linkage between process parameters - surface flatness - building quality for PBF-EB parts. In Section 3.2, we quantified the variation in surface quality metrics using values of surface flatness (Sa and Sdr) as the quantitative criterion used to describe the three surface qualities of PBF-EB parts, i.e. even surface, uneven surface and porous surface. Among these, a quantitative criterion of Sdr < 0.015 distinguishes good surface quality (even surface) of the part from bad surface quality (uneven surface or porous surface). By using this quantitative criterion to classify the surface quality of parts, the errors associated with the classification by human judgment are greatly reduced. Moreover, these quantitative criteria, obtained by non-destructive methods, can be determined by real-time monitoring during PBF-EB process. In Section 3.3, the results show that different surface qualities correspond to different internal defects, which allows the surface quality and internal defects of a part to be linked qualitatively. In Section 3.4, we have simulated the melt pool for different energy inputs, which further reveals the mechanism and correspondence between the formation of surface quality and internal defects. Although the results of the simulations are not directly applicable to the new framework, the description of the mechanism provides a scientific explanation and support for the construction of our new framework. In Section 3.5.1, the performance of several machine learning models commonly used for classification problems was evaluated and the optimal machine learning model (SVM) for use in this study was identified. The next discussion will focus on how to combine the new quantitative criterion for surface flatness (Sdr) and SVM to construct a processing map that can directly predict the processing parameters of a sample without internal defects.

To guide the design of PBF-EB process parameters, we used the SVM to construct a multidimensional process map of the PBF-EB process, which was first applied by Aoyagi et al. [21] and proven to be simple and effective. The advantage of this SVM optimization method is that the classification performance is not of primary importance because the method is predicting situations that are far from the decision boundary. The conditions near the decision boundary are easily affected by processing disturbances and instability of the building system, and the classification performance of the machine learning model depends largely on the classification accuracy of the data points near the decision boundary. The optimization method selects parameters that are far from the decision boundary, which is a good solution to the problem of poor model performances due to small number of datasets. In this prediction model, an SVM classification was conducted using the scikit-learn package. First, the attribute values in the training dataset were pre-processed using the StandardScaler function (a data standardization method) in the scikit-learn package to normalize the data to a standard normal distribution with a zero-mean and unit variance. The hyper-parameters were then optimized using the grid search procedure and the best optimal hyper-parameters were used for the classification of the SVM and the subsequent visualization of the processing map. Fig. 18 shows the cross-sections of the multidimensional process map constructed using SVM to classify the data in Table 4. The upper and lower bounds of the process parameters in these cross-sections are not the true upper and lower bounds, and the bounds in Fig. 18 depend on the processing range of the dataset used for machine learning. In these cross-sections, the blue area with a value of > 0.5, the process window for parts without internal defects, and the red area with a value of < 0.5 is the process condition for parts with internal defects. The process parameters for the internal defect-free parts in Fig. 18 are current of 2.5–10 mA, scan speed of 200–1000 mm/s, and line offset of 0.11–0.25 mm, or current of 2.5–10 mA, scan speed of 200–750 mm/s, and line offset of 0.27–0.33 mm. These process parameters can be used directly as input to the AM machine, and this method to construct a multidimensional process map greatly improves efficiency and reduces optimization costs. Traditional parameter optimization processes can only determine the goodness of a limited number of parameters for a specific setup, rather than thoroughly covering the entire window for internal defect-free parts in a multidimensional processing parameter space [51–56]. To verify the accuracy of these processing parameters, a random set of parameters (current = 6.67 mA, scan speed = 300 mm/s, and line offset = 0.30 mm) from the blue area (current = 2.5–10 mA, scan speed = 200–1000 mm/s, line offset = 0.11–0.25 mm, or current = 2.5–10 mA, scan speed = 200–750 mm/s, line offset = 0.27–0.33 mm) was selected for printing, and the fabricated samples were tested by 3D measurement and X-ray CT, and the results are shown in Fig. 19. The samples are even surface with Sdr = 0.004 and have no internal defects, indicating that this process map is very accurate and effective in the PBF-EB process.

A new framework for predicting the processing window of PBF-EB fabricated parts without internal defects is proposed, which comprises the following steps: the first step is to determine the process parameters using a uniform experimental design, thereby facilitating obtaining a dataset of process parameters uniformly distributed in a high-dimensional space; the second step is to fabricate parts with the process parameters determined in the first step; the third step) to observe the surface of the parts and classify them into two categories: good (without internal defects) or bad (with internal defects) based on the Sdr value of the part as a quantitative criterion; the final step is to use the

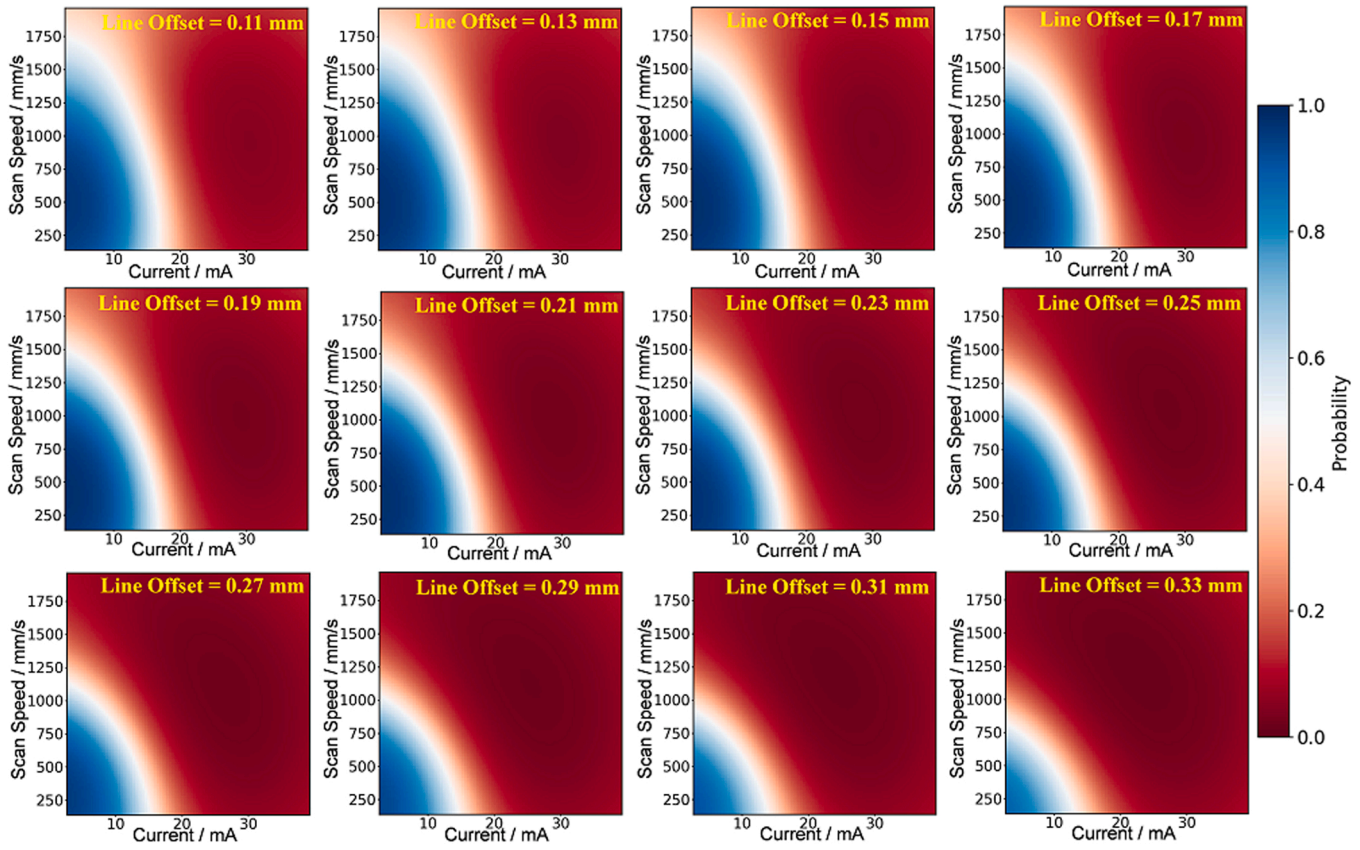

Fig. 18. Cross-sections of multidimensional process map constructed by using SVM as functions of scan speed, current and line offset. Dark blue (probability: 1.0) indicates that the surface morphology of the part printed by the processing parameters is predicted to be good (even) surface without internal defects, and dark red (probability: 0.0) indicates the bad (uneven or porous) surface with internal defects.

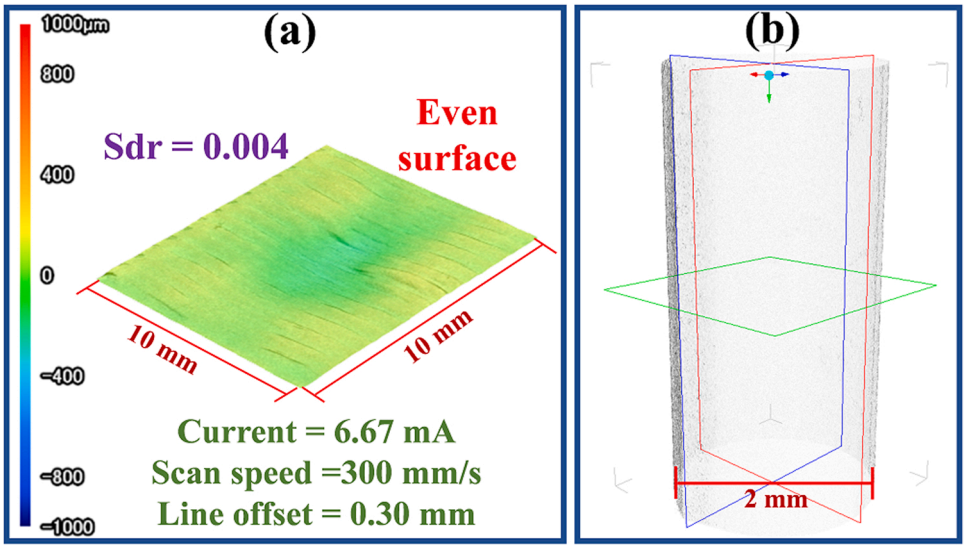

Fig. 19. (a) Three-dimensional surface topographical images of a part built under a randomly selected process condition (current = 6.67 mA, scan speed = 300 mm/s, and line offset = 0.30 mm) in the blue area of Fig. 18. (b) Three-dimensional rendering of X-ray CT analysis corresponding to the part in (a).

data classified by the Sdr value in the third step to select the machine learning technique with excellent performance and use it for the construction of the process map. This is an effective method for accelerating PBF-EB for manufacturing parts without internal defects.

4. Conclusion

In this study, the surface morphology of S30C alloys fabricated by PBF-EB was examined and classified using several types of surface flatness values. The relation between the internal defects and the surface morphology was revealed. The surface flatness values were used as a quantitative criterion to classify parts, and the results of that part

classification were used in an optimal machine learning model to construct a process map for parts without internal defects. The conclusions are as follows.

(1) A quantitative criterion for judging surface quality based on surface flatness was deduced as follows: Sdr $<$ 0.015 for an even surface; Sa $\geq$ 80 μm for an uneven surface; Sdr $\geq$ 0.015 and Sa $<$ 80 μm for porous surfaces. By using this quantitative criterion to classify the surface quality of parts, the errors associated with the classification by human judgment are greatly reduced.
(2) The type of internal defects was related to the surface morphology as follows: uneven surface parts included spherical pores, and porous surface parts included unmelted powder and irregular-shaped defects, the difference in energy input and the accumulation effect of layer-by-layer are the main reasons. Even surface parts were free of internal defects and had the highest density(7.7962 g/cm^3).
(3) The optimal energy input provided an even surface without internal defects. Excessive energy input provided an uneven surface with spherical pores, which could be due to vaporization and the residual of pores in the gas-atomized powder. Insufficient energy input provided a porous surface with unmelted powders and irregularly shaped defects.
(4) When the energy input is excessively high, the combination of the Marangoni effect, vapor recoil pressure, and electron beam agitation leads to a high velocity flow of liquid, which tends to form bumps, resulting in an uneven surface. Conversely, if the energy input is too low, the depth of the melt pool is too small to penetrate the thickness of the powder layers, resulting in incomplete melting of the powder at the bottom of the layers and the formation of defects due to lack of fusion between the layers.
(5) Five types of machine learning techniques were compared. Among these, the SVM model exhibited the highest model performance. The predicted optimal PBF-EB process parameter ranges for S30C alloy were as follows: current = 2.5–10 mA, scan speed = 200–1000 mm/s, line offset = 0.11–0.25 mm, or current = 2.5–10 mA, scan speed = 200–750 mm/s, line offset = 0.27–0.33 mm. These parameter ranges can be used as a choice of parameters for further printing of carbon steels with excellent mechanical properties in the future.
(6) A new framework for constructing a process map of PBF-EB fabricated parts was proposed, which is an effective method to accelerate PBF-EB for manufacturing parts without internal defects.

CRediT authorship contribution statement

Yunwei Gui: Writing – original draft, Visualization, Validation, Investigation. **Aoyagi Kenta:** Writing – review & editing, Supervision, Resources, Methodology, Funding acquisition, Conceptualization. **Huakang Bian:** Writing – review & editing. **Akihiko Chiba:** Supervision.

Declaration of Competing Interest

The authors declare that they have no known competing financial interests or personal relationships that could have appeared to influence the work reported in this paper.

Acknowledgments

This study was based on the results obtained from a project, JPNP19007, commissioned by the New Energy and Industrial Technology Development Organization (NEDO). This work was also supported by JSPS KAKENHI (Proposal No. 21K03801) and the Inter-University Cooperative Research Program (Proposal Nos. 18G0418, 19G0411, and 20G0418) of the Cooperative Research and Development Center for Advanced Materials, Institute for Materials Research, Tohoku University. Yunwei Gui would like to acknowledge financial support from the China Scholarship Council (Grant No. 201908410208).

Appendix A. Supplementary material

Supplementary data associated with this article can be found in the online version at doi:10.1016/j.addma.2022.102736.

References

[1] T. DebRoy, H.L. Wei, J.S. Zuback, T. Mukherjee, J.W. Elmer, J.O. Milewski, A. M. Beese, A. Wilson-Heid, A. De, W. Zhang, Additive manufacturing of metallic components – process, structure and properties, Prog. Mater. Sci. 92 (2018) 112–224, https://doi.org/10.1016/j.pmatsci.2017.10.001.
[2] N.T. Aboulkhair, M. Simonelli, L. Parry, I. Ashcroft, C. Tuck, R. Hague, 3D printing of aluminium alloys: additive manufacturing of aluminium alloys using selective laser melting, Prog. Mater. Sci. 106 (2019), 100578, https://doi.org/10.1016/j.pmatsci.2019.100578.
[3] A. Paolini, S. Kollmannsberger, E. Rank, Additive manufacturing in construction: a review on processes, applications, and digital planning methods, Addit. Manuf. 30 (2019), 100894, https://doi.org/10.1016/j.addma.2019.100894.
[4] H. Wang, X. Zhang, G.B. Wang, J. Shen, G.Q. Zhang, Y.P. Li, M. Yan, Selective laser melting of the hard-to-weld IN738LC superalloy: Efforts to mitigate defects and the resultant microstructural and mechanical properties, J. Alloy. Compd. 807 (2019), https://doi.org/10.1016/j.jallcom.2019.151662.
[5] X. Qi, N. Takata, A. Suzuki, M. Kobashi, M. Kato, Laser powder bed fusion of a near-eutectic Al–Fe binary alloy: processing and microstructure, Addit. Manuf. 35 (2020), 101308, https://doi.org/10.1016/j.addma.2020.101308.
[6] M. Liu, S. Liu, W. Chen, C. Chen, Y. Lv, X. Zhang, P. Lei, Y. Lin, K. Zhou, Effect of trace lanthanum hexaboride on the phase, grain structure, and texture of electron beam melted Ti-6Al-4V, Addit. Manuf. 30 (2019), 100873, https://doi.org/10.1016/j.addma.2019.100873.
[7] A. Gupta, C.J. Bennett, W. Sun, The role of defects and characterisation of tensile behaviour of EBM Additive manufactured Ti-6Al-4V: an experimental study at elevated temperature, Eng. Fail. Anal. 120 (2021), 105115, https://doi.org/10.1016/j.engfailanal.2020.105115.
[8] M. Galati, L. Iuliano, A literature review of powder-based electron beam melting focusing on numerical simulations, Addit. Manuf. 19 (2018) 1–20, https://doi.org/10.1016/j.addma.2017.11.001.
[9] S. Chandrasekar, J.B. Coble, S. Yoder, P. Nandwana, R.R. Dehoff, V.C. Paquit, S. S. Babu, Investigating the effect of metal powder recycling in electron beam powder bed fusion using process log data, Addit. Manuf. 32 (2020), https://doi.org/10.1016/j.addma.2019.100994.
[10] C. Wang, X. Tan, E. Liu, S.B. Tor, Process parameter optimization and mechanical properties for additively manufactured stainless steel 316L parts by selective electron beam melting, Mater. Des. 147 (2018) 157–166, https://doi.org/10.1016/j.matdes.2018.03.035.
[11] A. Bauereiß, T. Scharowsky, C. Körner, Defect generation and propagation mechanism during additive manufacturing by selective beam melting, J. Mater. Process. Technol. 214 (2014) 2522–2528, https://doi.org/10.1016/j.jmatprotec.2014.05.002.
[12] N. Sanaei, A. Fatemi, Defects in additive manufactured metals and their effect on fatigue performance: a state-of-the-art review, Prog. Mater. Sci. 117 (2021), 100724, https://doi.org/10.1016/j.pmatsci.2020.100724.
[13] I. Yadroitsev, I. Yadroitsava, A step-by-step guide to the L-PBF process. Fundamentals of Laser Powder Bed Fusion of Metals, 2021, pp. 39–77, https://doi.org/10.1016/B978-0-12-824090-8.00026-3.
[14] N.S. Johnson, P.S. Vulimiri, A.C. To, X. Zhang, C.A. Brice, B.B. Kappes, A. P. Stebner, Invited review: Machine learning for materials developments in metals additive manufacturing, Addit. Manuf. 36 (2020), https://doi.org/10.1016/j.addma.2020.101641.
[15] Q. Liu, H. Wu, M.J. Paul, P. He, Z. Peng, B. Gludovatz, J.J. Kruzic, C.H. Wang, X. Li, Machine-learning assisted laser powder bed fusion process optimization for AlSi10Mg: New microstructure description indices and fracture mechanisms, Acta Mater. 201 (2020) 316–328, https://doi.org/10.1016/j.actamat.2020.10.010.
[16] N. Hertlein, S. Deshpande, V. Venugopal, M. Kumar, S. Anand, Prediction of selective laser melting part quality using hybrid Bayesian network, Addit. Manuf. 32 (2020), 101089, https://doi.org/10.1016/j.addma.2020.101089.
[17] S. Liu, A.P. Stebner, B.B. Kappes, X. Zhang, Machine learning for knowledge transfer across multiple metals additive manufacturing printers, Addit. Manuf. 39 (2021), 101877, https://doi.org/10.1016/j.addma.2021.101877.
[18] Y.W. Luo, B. Zhang, X. Feng, Z.M. Song, X.B. Qi, C.P. Li, G.F. Chen, G.P. Zhang, Pore-affected fatigue life scattering and prediction of additively manufactured Inconel 718: an investigation based on miniature specimen testing and machine learning approach, Mater. Sci. Eng. A 802 (2021), https://doi.org/10.1016/j.msea.2020.140693.
[19] C. Wang, X.P. Tan, S.B. Tor, C.S. Lim, Machine learning in additive manufacturing: state-of-the-art and perspectives, Addit. Manuf. 36 (2020), 101538, https://doi.org/10.1016/j.addma.2020.101538.

[20] S. Nasiri, M.R. Khosravani, Machine learning in predicting mechanical behavior of additively manufactured parts, J. Mater. Res. Technol. 14 (2021) 1137–1153, https://doi.org/10.1016/J.JMRT.2021.07.004.
[21] K. Aoyagi, H. Wang, H. Sudo, A. Chiba, Simple method to construct process maps for additive manufacturing using a support vector machine, Addit. Manuf. 27 (2019) 353–362, https://doi.org/10.1016/j.addma.2019.03.013.
[22] C. Qiu, C. Panwisawas, M. Ward, H.C. Basoalto, J.W. Brooks, M.M. Attallah, On the role of melt flow into the surface structure and porosity development during selective laser melting, Acta Mater. 96 (2015) 72–79, https://doi.org/10.1016/J.ACTAMAT.2015.06.004.
[23] C. Panwisawas, C.L. Qiu, Y. Sovani, J.W. Brooks, M.M. Attallah, H.C. Basoalto, On the role of thermal fluid dynamics into the evolution of porosity during selective laser melting, Scr. Mater. 105 (2015) 14–17, https://doi.org/10.1016/J.SCRIPTAMAT.2015.04.016.
[24] H. Gong, K. Rafi, H. Gu, T. Starr, B. Stucker, Analysis of defect generation in Ti–6Al–4V parts made using powder bed fusion additive manufacturing processes, Addit. Manuf. 1–4 (2014) 87–98, https://doi.org/10.1016/J.ADDMA.2014.08.002.
[25] S.M. Gaytan, L.E. Murr, F. Medina, E. Martinez, M.I. Lopez, R.B. Wicker, Advanced metal powder based manufacturing of complex components by electron beam melting, Mater. Technol. 24 (2009) 180–190, https://doi.org/10.1179/106678509×12475882446133.
[26] J. Schwerdtfeger, R.F. Singer, C. Körner, In situ flaw detection by IR-imaging during electron beam melting, Rapid Prototyp. J. 18 (2012) 259–263, https://doi.org/10.1108/13552541211231572.
[27] N. Boone, C. Zhu, C. Smith, I. Todd, J.R. Willmott, Thermal near infrared monitoring system for electron beam melting with emissivity tracking, Addit. Manuf. 22 (2018) 601–605, https://doi.org/10.1016/J.ADDMA.2018.06.004.
[28] H. Yue, H. Peng, R. Li, Y. Su, Y. Zhao, K. Qi, Y. Chen, Selective electron beam melting of TiAl alloy: metallurgical defects, tensile property, and determination of process window, Adv. Eng. Mater. 22 (2020) 1–9, https://doi.org/10.1002/adem.202000194.
[29] N.T. Aboulkhair, N.M. Everitt, I. Ashcroft, C. Tuck, Reducing porosity in AlSi10Mg parts processed by selective laser melting, Addit. Manuf. 1 (2014) 77–86, https://doi.org/10.1016/j.addma.2014.08.001.
[30] C. Qiu, C. Panwisawas, M. Ward, H.C. Basoalto, J.W. Brooks, M.M. Attallah, On the role of melt flow into the surface structure and porosity development during selective laser melting, Acta Mater. 96 (2015) 72–79, https://doi.org/10.1016/j.actamat.2015.06.004.
[31] D. Hu, R. Kovacevic, Sensing, modeling and control for laser-based additive manufacturing, Int. J. Mach. Tools Manuf. 43 (2003) 51–60, https://doi.org/10.1016/S0890-6955(02)00163-3.
[32] H.K. Rafi, T.L. Starr, B.E. Stucker, A comparison of the tensile, fatigue, and fracture behavior of Ti-6Al-4V and 15-5 PH stainless steel parts made by selective laser melting, Int. J. Adv. Manuf. Technol. 69 (2013) 1299–1309, https://doi.org/10.1007/s00170-013-5106-7.
[33] A. Mertens, S. Reginster, Q. Contrepois, T. Dormal, O. Lemaire, J. Lecomte-Beckers, Microstructures and mechanical properties of stainless steel AISI 316L processed by selective laser melting, in: THERMEC 2013, Trans Tech Publications Ltd, 2014, pp. 898–903, https://doi.org/10.4028/www.scientific.net/MSF.783-786.898.
[34] M. Mazur, P. Brincat, M. Leary, M. Brandt, Numerical and experimental evaluation of a conformally cooled H13 steel injection mould manufactured with selective laser melting, Int. J. Adv. Manuf. Technol. 93 (2017) 881–900, https://doi.org/10.1007/s00170-017-0426-7.
[35] K.T. Fang, D.K.J. Lin, Ch. 4. Uniform experimental designs and their applications in industry. Handbook of Statistics 22, 2003, pp. 131–170, https://doi.org/10.1016/S0169-7161(03)22006-X.
[36] A.S. for Testing, M.C.B. on Metal Powders, M.P. Products, A.S. for Testing, M.S.B.0. on Bearings, Standard Test Methods for Density of Compacted or Sintered Powder Metallurgy (PM) Products Using Archimedes' Principle, ASTM International, 2009. ⟨https://books.google.co.jp/books?id=G3IyMwEACAAJ⟩.
[37] J.D. Anderson, Governing equations of fluid dynamics, Comput. Fluid Dyn. (1992) 15–51, https://doi.org/10.1007/978-3-662-11350-9_2.
[38] C. Hirt, B. Nichols, Volume of fluid (VOF) method for the dynamics of free boundaries, J. Comput. Phys. 39 (1981) 201–225, https://doi.org/10.1016/0021-9991(81)90145-5.
[39] FLOW-3D® Version 11.2 [Computer software], Flow Science Incorporated, St. Fe, NM, 2017. ⟨https://www.flow3d.com⟩.
[40] Y. Zhao, Y. Koizumi, K. Aoyagi, D. Wei, K. Yamanaka, A. Chiba, Molten pool behavior and effect of fluid flow on solidification conditions in selective electron beam melting (SEBM) of a biomedical Co-Cr-Mo alloy, Addit. Manuf. 26 (2019) 202–214, https://doi.org/10.1016/j.addma.2018.12.002.
[41] H.L. Wei, T. Mukherjee, W. Zhang, J.S. Zuback, G.L. Knapp, A. De, T. DebRoy, Mechanistic models for additive manufacturing of metallic components, Prog. Mater. Sci. 116 (2021), https://doi.org/10.1016/j.pmatsci.2020.100703.
[42] G. Chen, S.Y. Zhao, P. Tan, J. Wang, C.S. Xiang, H.P. Tang, A comparative study of Ti-6Al-4V powders for additive manufacturing by gas atomization, plasma rotating electrode process and plasma atomization, Powder Technol. 333 (2018) 38–46, https://doi.org/10.1016/j.powtec.2018.04.013.
[43] A. Townsend, L. Pagani, P.J. Scott, L. Blunt, Introduction of a surface characterization parameter Sdr prime for analysis of re-entrant features, J. Nondestruct. Eval. 38 (2019) 1–10, https://doi.org/10.1007/s10921-019-0573-x.
[44] L. Pagani, A. Townsend, W. Zeng, S. Lou, L. Blunt, X.Q. Jiang, P.J. Scott, Towards a new definition of areal surface texture parameters on freeform surface: re-entrant features and functional parameters, Meas. J. Int. Meas. Confed. 141 (2019) 442–459, https://doi.org/10.1016/j.measurement.2019.04.027.
[45] Y.J. Liu, S.J. Li, H.L. Wang, W.T. Hou, Y.L. Hao, R. Yang, T.B. Sercombe, L. C. Zhang, Microstructure, defects and mechanical behavior of beta-type titanium porous structures manufactured by electron beam melting and selective laser melting, Acta Mater. 113 (2016) 56–67, https://doi.org/10.1016/j.actamat.2016.04.029.
[46] D. Dai, D. Gu, Effect of metal vaporization behavior on keyhole-mode surface morphology of selective laser melted composites using different protective atmospheres, Appl. Surf. Sci. 355 (2015) 310–319, https://doi.org/10.1016/j.apsusc.2015.07.044.
[47] R. Cunningham, A. Nicolas, J. Madsen, E. Fodran, E. Anagnostou, M.D. Sangid, A. D. Rollett, Analyzing the effects of powder and post-processing on porosity and properties of electron beam melted Ti-6Al-4V, Mater. Res. Lett. 5 (2017) 516–525, https://doi.org/10.1080/21663831.2017.1340911.
[48] A.R. Balachandramurthi, J. Moverare, N. Dixit, R. Pederson, Influence of defects and as-built surface roughness on fatigue properties of additively manufactured Alloy 718, Mater. Sci. Eng. A 735 (2018) 463–474, https://doi.org/10.1016/j.msea.2018.08.072.
[49] P. Wang, M.L. Sharon Nai, X. Tan, G. Vastola, S. Raghavan, W.J. Sin, S.B. Tor, Q.X. Pei, J. Wei, Recent progress of additive manufactured Ti-6Al-4V by electron beam melting, in: Proceedings of the 27th Annual International Solid Freeform Fabrication Symposium – An Additive Manufacturing Conference, SFF 2016, 2016, pp. 691–704.
[50] H. Dalianis, Evaluation metrics and evaluation. Clinical Text Mining, Springer, Cham, 2018, https://doi.org/10.1007/978-3-319-78503-5_6.
[51] E. Ramirez-Cedillo, M.J. Uddin, J.A. Sandoval-Robles, R.A. Mirshams, L. Ruiz-Huerta, C.A. Rodriguez, H.R. Siller, Process planning of L-PBF of AISI 316L for improving surface quality and relating part integrity with microstructural characteristics, Surf. Coat. Technol. 396 (2020), 125956, https://doi.org/10.1016/j.surfcoat.2020.125956.
[52] H.J. Lee, H.K. Kim, H.U. Hong, B.S. Lee, Influence of the focus offset on the defects, microstructure, and mechanical properties of an Inconel 718 superalloy fabricated by electron beam additive manufacturing, J. Alloy. Compd. 781 (2019) 842–856, https://doi.org/10.1016/j.jallcom.2018.12.070.
[53] X. Ding, Y. Koizumi, K. Aoyagi, T. Kii, N. Sasaki, Y. Hayasaka, K. Yamanaka, A. Chiba, Microstructural control of alloy 718 fabricated by electron beam melting with expanded processing window by adaptive offset method, Mater. Sci. Eng. A 764 (2019), 138058, https://doi.org/10.1016/j.msea.2019.138058.
[54] W. Ge, C. Guo, F. Lin, Effect of process parameters on microstructure of TiAl alloy produced by electron beam selective melting, Procedia Eng. 81 (2014) 1192–1197, https://doi.org/10.1016/j.proeng.2014.10.096.
[55] K. Vutova, V. Vassileva, E. Koleva, V. Stefanova, D.P. Amalnerkar, Effects of process parameters on electron beam melting technogenic materials for obtaining rare metals, J. Phys. Conf. Ser. 1089 (2018), https://doi.org/10.1088/1742-6596/1089/1/012013.
[56] T. Kurzynowski, M. Madeja, R. Dziedzic, K. Kobiela, The effect of EBM process parameters on porosity and microstructure of Ti-5Al-5Mo-^{5}V–^{1}Cr-1Fe alloy, Scanning (2019) (2019), https://doi.org/10.1155/2019/2903920.